A role for MIRO1 in motility and membrane dynamics of peroxisomes

Inês Gomes Castro[1, †], David Mark Richards[2], Jeremy Metz[1], Joseph Liam Costello[1], Josiah Benjamin Passmore[1], Tina Angelika Schrader[1], Ana Gouveia[3], Daniela Ribeiro[3], Michael Schrader[1]

[1]Biosciences and [2]LSI, University of Exeter, Exeter EX4 4QD, UK

[3]Institute of Biomedicine, University of Aveiro, Aveiro 3810-193, Portugal

[†]Present: Dept. of Molecular Genetics, Weizmann Institute of Science, Rehovot 7610001, Israel

Correspondence: M.Schrader@exeter.ac.uk

Running title: MIRO1-mediated peroxisome dynamics and motility

Synopsis (for table of contents, max 80 words): Peroxisome motility in mammalian cells is still a poorly understood process, and its physiological importance for organelle function and dynamics is unknown. Here, we show that the Mitochondrial Rho GTPase 1 (MIRO1) is targeted to peroxisomes where it can alter organelle distribution by microtubule-dependent motility. Expression of this protein in cellular models of peroxisome disease has an impact on peroxisome membrane elongation and division, supporting the notion that motility is an essential element for modulation of the peroxisomal compartment and function.

Keywords: MIRO1, organelle motility, peroxisome, microtubule, membrane protrusion, proliferation, mathematical modelling

Abbreviations: TA, tail-anchored; TMD, transmembrane domain; WT, wild type.

Author contributions

JBP, TAS, AG performed experiments and analysed data; MS, IGC, JM, JLC, DMR, DR conceived the project, performed experiments, analysed data; MS, IGC, JLC, JM and DMR wrote the manuscript; all authors contributed to methods.

Abstract

Peroxisomes are dynamic organelles which fulfil essential roles in lipid and ROS metabolism. Peroxisome movement and positioning allows interaction with other organelles and is crucial for their cellular function. In mammalian cells, such movement is microtubule-dependent and mediated by kinesin and dynein motors. The mechanisms of motor recruitment to peroxisomes are largely unknown, as well as the role this plays in peroxisome membrane dynamics and proliferation. Here, using a combination of microscopy, live-cell imaging analysis and mathematical modelling, we identify a role for the Ras GTPase MIRO1 as an adaptor for microtubule-dependent peroxisome motility in mammalian cells. We show that MIRO1 is targeted to peroxisomes and alters their distribution and motility. Using a peroxisome-targeted MIRO1 fusion protein, we demonstrate that MIRO1-mediated pulling forces contribute to peroxisome membrane elongation and proliferation in cellular models of peroxisome disease. Our findings reveal a molecular mechanism for establishing peroxisome-motor protein associations in mammalian cells and provide new insights into peroxisome membrane dynamics in health and disease.

Introduction

Peroxisomes are dynamic, multifunctional organelles that vary in size, number, and shape depending on cell type, environmental stimuli and metabolic demand [1], but the underlying molecular mechanisms which govern this versatility are not fully understood. Similar to mitochondria, peroxisomes are oxidative organelles that fulfil important functions in lipid metabolism and ROS homeostasis rendering them essential for human health and development [2,3]. Peroxisomes metabolically cooperate and physically interact with a variety of subcellular organelles including the ER, mitochondria, lipid droplets and other peroxisomes [4–6]. These functions require peroxisome positioning and movement within eukaryotic cells.

Whereas in yeast and plant cells peroxisome motility depends on actin filaments and myosin motors [7,8], in mammalian cells peroxisomes move bidirectionally via microtubules, using both kinesin and dynein motors [9–12]. The shape and number of peroxisomes is controlled by PEX11β, a peroxisomal membrane protein, which induces elongation and remodelling of the peroxisomal membrane and acts as a GTPase activating protein on the large fission GTPase DNM1L [13–15]. Loss of PEX11β was recently linked to spindle misorientation and peroxisome mislocalisation in mitosis causing imbalances in epidermal differentiation [16]. These findings underline the importance of peroxisome multiplication, distribution and inheritance for cell fate decisions.

Although key factors required for peroxisome dynamics and multiplication have been identified, it is currently unclear to what extent cytoskeletal tracks, docking factors and pulling forces mediated by associated motor proteins contribute to these processes, in particular in mammals [17]. In baker's yeast, peroxisome distribution and inheritance depends on actin, the myosin motor Myo2 and specific adaptor proteins, Inp1 and Inp2, at the peroxisomal membrane [7]. Furthermore, the peroxins Pex3 and Pex19 have been found to interact with myosin motors [18,19]. In contrast, little is known about the recruitment of microtubule motors to peroxisomes in mammalian cells [20].

Here, we identify the Ras GTPase MIRO1 as a potential adaptor for microtubule-based peroxisome motility in mammalian cells. MIRO proteins were initially identified on the outer mitochondrial membrane [21] where they, together with TRAK1/2, link the microtubule motors kinesin and dynein to mitochondria [22–25], and play key roles in

mitochondrial motility, homeostasis, and inheritance [26,27]. Mammalian MIRO1 and MIRO2 share 60% similarity and an analogous structure containing two GTPase and two EF-hand calcium binding domains [21,28]. Studies on mammalian MIRO proteins have focused mainly on MIRO1 due to its clear role in mitochondrial motility, particularly in neurons [22,25]. Loss of MIRO1-directed mitochondrial movement and distribution result in neurological defects [26]. MIRO1-mediated mitochondrial positioning is also suggested to shape intracellular energy gradients required for cell migration [29]. We show that MIRO1 localises to peroxisomes and mitochondria, and alters peroxisome distribution and motility. Furthermore, we demonstrate that an exclusively peroxisome-targeted MIRO1 can mediate pulling forces which contribute to peroxisome membrane elongation and proliferation in a cell type-dependent manner. To better understand the versatility of peroxisomes in mammalian cells, we build a first mathematical model of peroxisome dynamics. This model helps to explain the underlying principles of peroxisome morphologies induced by MIRO1-mediated pulling forces and other factors which influence peroxisomal membrane dynamics.

Results

MIRO1 is dually targeted to peroxisomes and mitochondria

Previous studies revealed a dual mitochondrial and peroxisomal localisation of several C-tail anchored (TA) membrane proteins including FIS1, MFF, and GDAP1, which function in peroxisomal and mitochondrial division [30–33]. In a recent study on the targeting of TA proteins to different organelles, we provided preliminary evidence for a dual peroxisomal and mitochondrial localisation of the Ras GTPases MIRO1 and MIRO2 [34]. MIRO1 was initially identified on the outer mitochondrial membrane [21], and forms a protein complex with TRAK1/2 that includes both kinesin and dynein motors, promoting mitochondrial movement through the microtubule cytoskeleton [22–25]. A dual mitochondrial and peroxisomal localisation of MIRO1 was confirmed by immunofluorescence after expression of Myc-MIRO1 in COS-7 cells (Fig. 1A). Further, we previously reported endogenous MIRO1 in highly purified peroxisomal and mitochondrial fractions [34], in agreement with proteomics data [35,36].

The targeting of all known TA proteins to peroxisomes requires the peroxisomal import receptor/chaperone PEX19 [34]. For MIRO1, PEX19 binding was shown by immunoprecipitation after co-expression of Myc-MIRO1 and HA-PEX19 in COS-7 cells (Fig. 1B) suggesting a role for PEX19 in the targeting of MIRO1 to peroxisomes. Additionally, in a high-throughput interaction study, MIRO1 was identified as a PEX19 interaction partner [37]. These findings are also consistent with the known organelle targeting signals: MIRO1 possesses a transmembrane domain (TMD) with relatively low hydrophobicity (GRAVY, 1.3) and a moderate net charge in the tail region (1.9), which based on our previous work would be indicative of a TA protein that localises predominantly to mitochondria but has a potential for peroxisomal targeting [34]. Overall, our findings support a dual localisation of MIRO1 at mitochondria and peroxisomes.

MIRO1 alters peroxisome distribution in COS-7 cells

MIRO1 has been shown to play a key role in mitochondrial motility and distribution in mammalian cells [26]. To determine if MIRO1 also plays a role in peroxisome positioning we expressed Myc-tagged wild type (WT) and mutated versions in COS-7 cells, and analysed their effect on peroxisome distribution (Fig. 1A, C; Suppl. Fig. S1). As

previously described [21,38], the expression of Myc-MIRO1 resulted in abnormal mitochondrial morphologies (Fig.1A; Suppl. Fig. S1). To avoid potential secondary effects due to dysfunctional mitochondria, we generated an exclusively peroxisomal set of MIRO1 proteins by altering the C-terminal TMD using a previously described PEX26/ALDP construct (Fig. 1C) [39]. Expression of the resulting Myc-MIRO1^{Pex} fusion protein in COS-7 cells revealed an exclusively peroxisomal localisation, with no effects on mitochondrial morphology and distribution (Fig. 1D, E). Peroxisomes in COS-7 cells usually distribute uniformly throughout the cytoplasm [30,40]. Interestingly, expression of Myc-MIRO1^{Pex} or Myc-MIRO1$^{V13\text{-}Pex}$, a constitutively active GTPase mutant, induced peroxisome re-distribution and accumulation at the cell periphery (Fig. 1D, F, G). On the other hand, expression of dominant negative Myc-MIRO1$^{N18\text{-}Pex}$ and EF-hand mutant Myc-MIRO1$^{KK\text{-}Pex}$ resulted in peroxisome accumulations which were scattered throughout the cytoplasm (Fig. 1F, G). Comparable results were obtained with the dually targeted MIRO1 versions (Suppl. Fig. S1B). Myc-MIRO1$^{\Delta TM}$, a version lacking the TMD/tail sequence, localised to the cytoplasm and had no effect on peroxisome distribution, indicating that membrane anchorage is required for MIRO1 function (Suppl. Fig. S1). Furthermore, depolymerisation of microtubules with nocodazole in Myc-MIRO1^{Pex} expressing cells abolished accumulation of peroxisomes in the cell periphery, suggesting that an intact microtubule cytoskeleton is required for peroxisome distribution via MIRO1 (Suppl. Fig. S2A). Our findings indicate that, similarly to its role on mitochondria, MIRO1 can alter peroxisome distribution and positioning by affecting microtubule-dependent peroxisome motility.

Peroxisomal MIRO1 increases movement of peroxisomes

To quantify the effect of MIRO1 expression on peroxisome motility, live-cell imaging experiments were performed with COS-7 cells expressing Myc-MIRO1$^{V13\text{-}Pex}$ and the peroxisome marker EGFP-SKL (Fig. 2A-C; Suppl. Videos S1, S2). To measure movement, peroxisomes were automatically detected and tracked using a customized in-house algorithm [41]. To visualize displacement, 100 trajectories were randomly sampled and plotted from a central point (Fig. 2A). Expression of Myc-MIRO1$^{V13\text{-}Pex}$ significantly increased peroxisome displacement. Fig. 2B displays the empirical cumulative distribution function (ECDF) of the instantaneous peroxisome speeds for

all peroxisomes analysed with each point of the curve corresponding to a single movement. For this analysis, all speed values above 0.24 µm/s were considered microtubule-dependent movements as previously described [42]. A significant increase in the number of fast moving peroxisomes can be observed in cells expressing Myc-MIRO1$^{V13\text{-}Pex}$ (Fig. 2B, C; Suppl. Videos S1, S2). Whereas in control cells 5.2 ± 0.7% of peroxisomes moved in a microtubule-dependent manner, in cells expressing Myc-MIRO1$^{V13\text{-}Pex}$ this number increased to 14.0 ± 2.0% (Fig. 2C). Imaging of peroxisome accumulations at the cell periphery revealed that while the organelles appear to be confined to a relatively restricted area of the cell, peroxisomes regularly move within these accumulations, revealing dynamic interactions (Suppl. Video S2). To examine the effect of a loss of MIRO1 function on peroxisome distribution and motility, we analysed MIRO1 KO MEFs (Suppl. Fig. S2B-E). These cells have an altered mitochondrial distribution but peroxisome morphology and distribution appeared to be unaffected [43]. In agreement with those findings, we did not detect any alterations in peroxisome distribution (Suppl. Fig. S2C) or motility (Suppl. Fig. S2D, E). These findings indicate that when targeted to peroxisomes in COS-7 cells, active MIRO1, a known adaptor for the microtubule plus-end motor kinesin, can re-distribute peroxisomes to the cell periphery (where microtubule plus ends are located) in a microtubule-dependent manner. However, MIRO1 may not be the only adaptor for microtubule-dependent motor proteins at peroxisomes, as its loss is apparently not essential to maintain peroxisome distribution and motility. It is possible that MIRO2, which also localises to peroxisomes [34], can complement loss of MIRO1. Furthermore, peroxisomes may tether to or “hitchhike” other moving organelles to maintain their distribution. The latter process has been observed in filamentous fungi [44].

MIRO1 induces peroxisome proliferation in human skin fibroblasts

The peroxisome-targeted MIRO1 represents a new tool to manipulate peroxisome motility and to exert motor-driven pulling forces at peroxisomes under control and disease conditions. Peroxisomes in fibroblasts from patients with peroxisomal disorders are often enlarged and reduced in number, and tend to cluster and detach from microtubules [45]. We first expressed Myc-MIRO1^{Pex} in human skin fibroblasts from a healthy control and examined its effect on the peroxisomal compartment (Fig. 2D).

Surprisingly, in these cells peroxisomes did not accumulate at the cell periphery but instead proliferated, presenting a significant increase in number (mean peroxisome number/cell: control 740 ± 50; Myc-MIRO1^{Pex} 1040 ± 100, n= 24) (Fig. 2E). In addition, the percentage of motile peroxisomes that moved in a microtubule-dependent manner was significantly increased (Fig. 2F; Suppl. Fig. S2F) (Suppl. Videos S3, S4). These findings indicate that MIRO1-bound motor proteins can exert forces at peroxisomes, which result in peroxisome division, thus increasing peroxisome number. Separation by pulling forces is only possible when the peroxisome is tethered to another structure, as it would otherwise simply move in the direction of the pulling force (Fig. 4B). This untethered motion is observed in COS-7 cells, where MIRO1 expression accumulates peroxisomes in the cell periphery where microtubule-plus ends are located (Figs. 1, 4B). We recently revealed that peroxisome-ER membrane contacts are mediated by peroxisomal ACBD5 that interacts with ER-resident VAPB to form a peroxisome-ER tether [46]. Loss of ACBD5 increased the movement of peroxisomes in human skin fibroblasts, indicating that peroxisome-ER membrane contacts restrict peroxisome motility. In line with this, our analyses reveal that the percentage of fast moving peroxisomes in control fibroblasts is lower than that in control COS-7 cells (4.5 ± 0.4% vs 5.2 ± 0.7%). We suggest that peroxisome-ER tethering is cell-type specific and that MIRO1/motor-mediated pulling forces can induce peroxisome proliferation in fibroblasts, whereas in COS-7 cells peroxisomes are dragged towards the cell periphery (Fig. 4B). These findings indicate that a close interplay between tethering and motile forces modulates not only peroxisome distribution but also proliferation.

To analyse the impact of MIRO1 expression on peroxisomes in patient fibroblasts, we expressed Myc-MIRO1^{Pex} in PEX5 and PEX14 deficient cells. PEX5 and PEX14 are proteins of the peroxisomal matrix protein import machinery, and loss of function leads to “empty” membrane structures (so called “ghosts”) that lack peroxisomal enzymes and are metabolically inactive. Peroxisomes in those cells are often enlarged and reduced in number (Fig. 2D). Expression of Myc-MIRO1^{Pex} in both PEX5 and PEX14 deficient cells induced peroxisome proliferation, but many peroxisomes remained enlarged (Fig. 2D, E). MIRO1 expression also significantly increased peroxisome motility in patient cells (Fig. 2F; Suppl. Fig. S2G-H), most prominently for the smaller peroxisomes (Suppl. Videos S5-8). In contrast to a recent report we observed that peroxisomes in PEX14 deficient cells are motile [47]. These findings show that MIRO1-

mediated pulling forces can at least partially induce the proliferation of metabolically inactive peroxisomes, indicating that membrane components are the most relevant factors for this process.

Peroxisome-targeted MIRO1 promotes the formation of extended membrane protrusions in PEX5 deficient fibroblasts

Peroxisomes are highly dynamic organelles that can be found as spherical or elongated structures and also form membrane protrusions. These membrane alterations are suggested to contribute to peroxisome formation via division of elongated organelles, and to enable organelle crosstalk [1,48]. To what extent microtubule motors and pulling forces contribute to peroxisome membrane dynamics is unclear, as peroxisome elongation is unexpectedly promoted by microtubule-depolymerising drugs, and peroxisome division can occur in the absence of microtubules [9,49]. In PEX5 deficient fibroblasts expressing Myc-MIRO1^{Pex}, we observed long membrane protrusions emanating from large, spherical peroxisomes and following linear tracks with sporadic bends (Fig. 3A). These membrane protrusions co-localised with microtubules, indicating their formation is promoted by MIRO1/motor generated pulling forces along microtubules (Fig. 3B). Our observations also suggest the existence of as yet unidentified docking proteins which link peroxisomes to microtubules, and would facilitate the bending and directional changes we observe in the membrane protrusions. To analyse the dynamics of peroxisomal membrane protrusions, we performed time-lapse analyses of PEX5 deficient cells expressing Myc-MIRO1^{Pex} (Fig. 3C). We revealed that protrusions originating from large peroxisomes grow at varying speeds, generally form straight lines in a single direction (Fig. 3C-E) (Suppl. Video S9) and occasionally appear to interact with other peroxisomes (Fig. 3C). Transient peroxisome interactions, which may contribute to organelle crosstalk, have been previously reported [42]. Interestingly, these protrusions can sometimes quickly retract, suggesting that the peroxisomal membrane has elastic properties that are largely unexplored (Fig. 3C, D). A comparison of the surface area of a globular peroxisome from Zellweger fibroblasts (approx. 1 µm in diameter) [50] with an elongated membrane protrusion (approx. 20 µm in length, 80 nm in diameter) [14,46] indicates a 16 fold increase in the surface area of the protrusion. As it is unlikely that

the globular peroxisome on its own can provide sufficient membrane lipids to generate such a protrusion, additional membrane lipids are likely provided by the ER. In support of this, we have recently revealed that peroxisome-ER membrane contacts have an impact on peroxisomal membrane expansion [46]. Whereas protrusions were not observed in control fibroblasts, they were formed in PEX5 and PEX14 deficient cells under control conditions, albeit more frequently in PEX5 deficient cells (Fig. 3E). As peroxisomes are reduced in number in PEX5 and PEX14 deficient cells and are less motile than in controls, peroxisome protrusions may form to overcome those restrictions and to maintain organelle crosstalk. However, peroxisome metabolism is required to generate cellular lipids which are also necessary for peroxisome division and proliferation [51]. As PEX5 and PEX14 deficient cells lack peroxisomal metabolic functions, their ability to divide and proliferate peroxisomes is compromised, which may explain the formation and frequency of membrane elongations (Fig. 4B). Expression of Myc-MIRO1^{Pex}, however, significantly increased the frequency and length of protrusions in PEX5 deficient- but not in PEX14 deficient cells (Fig. 3E), suggesting that loss of PEX14 could interfere with the stability of membrane protrusions.

A mathematical model of peroxisome dynamics

To further understand the mechanisms involved in peroxisome dynamics, we developed a simple mathematical model that describes their growth and division. We used a stochastic, population-based modelling approach that describes the morphology of a group of individual peroxisomes. Each peroxisome consists of a body of radius r with an optional elongation of length L and diameter w (Fig. 4A a)). The size of the body and elongation are controlled by three basic processes (Fig. 4A b)): (i) a membrane lipid flow rate to the body (e.g. from the ER) (governed by rate α and lipid flow constant γ), (ii) an elongation growth rate (governed by speed v and minimum radius r_{min}), and (iii) a division rate proportional to the elongation length (governed by rate β and minimum length L_{min}). In addition, peroxisome turnover is controlled by the peroxisome mean lifetime τ. This leads to a model that is applicable to a range of experimental conditions (see Suppl. information for full model details). Using WT parameters, we obtained a phenotype that reflects the heterogeneous peroxisome

population observed in mammalian cells in terms of number, average body size and average elongation length (Fig. 4A c)). The WT division rate *β* is sufficiently high, resulting in division of peroxisome elongations shortly after formation. When considering a block in peroxisome division by setting the division rate *β* to almost zero, the model exhibits reduced numbers of peroxisomes all of which contain long elongations (Fig. 4A d)). Such a scenario is observed in patient fibroblasts lacking MFF, the membrane adaptor for the fission GTPase Drp1, where we would expect division rates to be significantly reduced [52,53]. The fact that changing only one parameter can capture this dramatic change in phenotype gives confidence that the model is able to correctly describe the basic processes involved in peroxisomal growth and division.

Next, we examined overexpression of MIRO1 in WT cells. For fibroblasts, we modelled this as a large increase (by a factor of 10) in the elongation growth rate *v* accompanied by an increase in lipid flow (modelled by halving the lipid flow constant *γ*). This leads to an increase in peroxisome number without a noticeable change in morphology, which is again explained by the fact that the WT division rate *β* causes almost all elongations to divide soon after formation, so that increased elongation growth rate and lipid flow can only result in proliferation (Figs. 2D; 4B b)). Conversely, in COS-7 cells, MIRO1 overexpression results in peroxisomes moving to the cell periphery (Figs. 1, 4B a)). We model this as an increase in *v* with no corresponding increase in lipid flow (e.g. due to reduced peroxisome-ER contact). Since lipid flow cannot keep up with the increased elongation speed, there is little impact on morphology or number, in agreement with our experimental observations.

The peroxisome phenotype in PEX5 deficient cells can be captured in the model by reducing both the division rate *β* and the elongation speed *v* (Fig. 4A e)), resulting in fewer and larger peroxisomes. This is in line with compromised peroxisome division and proliferation due to impaired peroxisomal lipid metabolism [51]. Modelling overexpression of MIRO1 in PEX5 deficient cells (by also increasing *v* and decreasing *γ*) recapitulates the phenotype we found experimentally, where a substantial proportion of peroxisomes contain long elongations (Fig. 4A f), 4B c)). Interestingly, this indicates that, despite a lack of peroxisomal metabolism, peroxisomal membranes retain their plasticity allowing lipid flow and membrane growth. Peroxisome proliferation in those cells is likely impaired due to reduced division rates (e.g. due to

altered peroxisomal membrane lipid composition). Whereas expression of MIRO1 cannot fully restore division, this can be achieved by PEX11β, a key factor in peroxisomal membrane remodelling and division [1] (Fig. 5A). Expression of PEX11β-EGFP in PEX5 deficient cells promoted peroxisome elongation and subsequent division (Fig. 5A) confirming earlier reports that PEX11β-induced peroxisome proliferation is independent of peroxisomal metabolism [45,54]. As PEX11β also activates the fission GTPase Drp1 [15], it likely increases the division rate β as well as the elongation speed v and lipid flow rate.

In mammalian cells peroxisomes can elongate independently of microtubules, and peroxisome elongation is promoted by microtubule-depolymerizing drugs [9,49]. This suggests that PEX11β and motor forces (e.g. mediated by MIRO1) can act independently to promote peroxisome proliferation, but may cooperate under physiological conditions. This assumption is supported by live-cell imaging of peroxisome dynamics in COS-7 cells expressing PEX11β-EGFP (Fig. 5B, C) [14]. Similar to PEX5 deficient cells, PEX11β-EGFP expression results in the formation of membrane protrusions emanating from globular peroxisomes. Occasionally, these peroxisomes show directed, long-range movements with the linear protrusion leading (Fig. 5C 28-40s; Suppl. Video S10). These structures resemble the globular peroxisomes and protrusions induced by MIRO1 via microtubule-dependent motor forces. Globular peroxisomes can become more static, either by docking to microtubules and/or tethering to other organelles such as the ER (66.2 ± 2.6% of peroxisomes in COS-7 cells are associated with the ER [46]) (Fig. 5C 42-54s; Suppl. Video S10). However, in contrast to the more static globular peroxisomes, the membrane protrusions show a more random, tentacle-like movement, which does not seem to be directed by microtubules (Fig. 5C 42-54s; Suppl. Video S10). This type of movement likely allows the peroxisomes to efficiently explore the environment and to engage with other organelles while being attached. Peroxisomes can then detach again and continue to move in a directed manner. Occasionally, membrane division is observed (Fig. 5C 135-141s; Suppl. Video S10). These observations indicate that different, but cooperating mechanisms contribute to peroxisome dynamics and proliferation: PEX11β enables peroxisome membrane protrusion via its membrane deforming and scaffolding properties, and subsequently leads to division whereas MIRO1 on the other hand can elongate and divide peroxisomes by pulling forces via

its interaction with microtubule-dependent motors. Both mechanisms can function independently, as peroxisomes can elongate and divide in the absence of microtubules, but adaptors such as MIRO1 and associated motors provide directionality to peroxisome membrane expansion and peroxisome movement.

Discussion

Our findings support a peroxisomal and mitochondrial localisation of MIRO1 and a role for MIRO1 in establishing peroxisome-motor protein associations in mammalian cells. As MIRO1 can alter peroxisome distribution and motility, it is likely one of the yet unidentified adaptors for microtubule-based peroxisome motility in mammalian cells. This assumption is further supported by recent findings showing that mitochondria and peroxisomes share many TA membrane proteins and their functions due to their close cooperation and co-evolution in mammalian cells [34]. During the submission of our work, Okumoto et al. (2017) [55] revealed that distinct MIRO1 splice variants show different targeting to mitochondria and peroxisomes in HEK cells, with MIRO1-variant 4 being more specific for peroxisomes. Peroxisomal MIRO1 also induced peroxisome accumulation and mediated long-range movement of peroxisomes along microtubules further supporting a role for MIRO1 in peroxisomal motility. In contrast to our findings, MIRO1-var1 localised primarily to mitochondria, which may be explained by the use of different cell lines or differences in expression levels of MIRO1.

We also show that peroxisome-targeted MIRO1 can be used as a tool to exert pulling forces at peroxisomes, and that MIRO1-mediated pulling forces have an impact on peroxisomal distribution, membrane dynamics and proliferation. These observations in combination with our mathematic model of peroxisome dynamics, shed light on the role of pulling forces in peroxisome formation by growth and division which have been controversial [9,17]. We show that MIRO1-mediated motor forces along microtubules can elongate and divide peroxisomes. As elongation and division can still occur in the absence of microtubules, we suggest that independent, but cooperative mechanisms exist, and that motor forces support membrane dynamics by providing directionality. This is now in agreement with observations in yeast, where actin-based, myosin-driven pulling forces cause peroxisome elongation and separation in dynamin mutants [56,57]. Our approaches also contribute to the understanding of the versatility of peroxisome

morphology in mammalian cells. In our model, we develop basic principles for peroxisome dynamics which govern peroxisome morphology. This helps us to understand why peroxisomes in division incompetent cells are highly elongated (due to continued lipid flow, e.g. from the ER, in the absence of membrane fission), and why MIRO1-mediated pulling forces can proliferate peroxisomes in fibroblasts (due to peroxisome-ER tethers which prevent movement to the cell periphery). It also contributes to our understanding of peroxisome phenotypes in disease, for example in PEX5 deficient cells from Zellweger patients. Here, metabolically compromised peroxisomes retain their plasticity and can elongate via MIRO1-mediated pulling forces, but proliferation is reduced, likely due to altered membrane lipids [51].

Despite their fundamental importance to cell physiology, the mechanisms that mediate and regulate peroxisomal membrane dynamics and abundance in humans are poorly understood. Our study aids in understanding these mechanisms which is not only important for comprehending fundamental physiological processes but also for understanding pathogenic processes in disease etiology.

Materials and Methods

Plasmids and antibodies

For cloning of peroxisome -targeted MIRO1, the C-terminal TMD and tail of Myc-MIRO1 was exchanged by a PEX26/ALDP fragment previously shown to target proteins to the peroxisomal membrane [39]. See Table S1 for details of plasmids used in this study, Table S2 for plasmids generated in this study and Table S3 for details of primers used. All constructs produced were confirmed by sequencing (Eurofins Genomics). Details on all antibodies used in this study can be found in Table S4.

Cell culture and transfection

COS-7 cells (ATCC CRL-1651), human control skin fibroblasts (C109), PEX5 and PEX14 deficient fibroblasts (kindly provided by H. Waterham, AMC, University of Amsterdam, NL and M. Fransen, KU Leuven, BE) were cultured in DMEM, high glucose (4.5 g/L) supplemented with 10% FBS, 100 U/ml penicillin and 100 µg/ml streptomycin at 37°C with 5% CO_2 and 95% humidity. WT and MIRO1 KO mouse

embryonic fibroblasts (MEF) (kindly provide by J. Shaw, University of Utah, USA) were cultured in the same media and supplemented with β-mercaptoethanol at a final concentration of 50 µM. COS-7 cells were transfected using TurboFect™ (Thermo Fisher Scientific). To analyse the effects of microtubule depolymerisation, cells were treated 24 h after transfection with 10 µM nocodazole (10 mM stock in DMSO), and incubated for 1 or 4 h before being fixed. Control cells were incubated with the same volume of DMSO as that used to dissolve nocodazole (maximum 0.1% v/v). Fibroblasts were transfected by microporation using the Neon® Transfection System (Thermo Fisher Scientific) following the manufacturer's protocol. In short, cells (seeded 24 h prior to transfection) were washed once with PBS and trypsinized using TrypLE Express. Trypsinized cells were resuspended in complete media without antibiotics and centrifuged for 3 min at 1000 rpm, and the pellet washed with PBS. The cells were once again centrifuged and carefully resuspended in 10 µl Buffer R. For each condition, 10^5 cells were mixed with the DNA construct (1-2 µg). Cells were microporated using a 10 µl Neon tip with the following settings: 1700 V, 20 ms, 1 pulse (human fibroblasts); 1350 V, 30 ms, 1 pulse (MEFs). Microporated cells were immediately seeded into plates with pre-warmed complete medium without antibiotics and incubated at 37°C with 5% CO_2 and 95% humidity. For live-cell imaging, cells were co-transfected with a fluorescent PO marker (EGFP-SKL for COS-7 and EGFP-ACBD5^{TMD-T} for fibroblasts) at a 1:2 ratio with Myc-MIRO1^{Pex} plasmids. As peroxisomal matrix import is defective in PEX5 and PEX14 patient fibroblasts, we used a fusion of EGFP and the TMD/tail region of ACBD5 (EGFP-ACBD5^{TMD-T}) to label the peroxisomal membrane in control and patient cells.

Immunofluorescence and microscopy

Cells were processed for immunofluorescence 24 or 48 h after transfection. Cells grown on glass coverslips were fixed for 20 min with 4% PFA in PBS (pH 7.4), permeabilized with 0.2% Triton X-100 for 10 min and blocked with 1% BSA for 10 min. To visualize both PO and the microtubule network, cells were fixed for 10 min with 4% PFA followed by 5 min with ice-cold methanol. Blocked cells were sequentially incubated with primary and secondary antibodies for 1 h in a humid chamber (Table S4). Coverslips were washed with ddH_2O to remove PBS and mounted with Mowiol medium on glass slides. All immunofluorescence steps were performed at room temperature and cells were washed three times with PBS between each individual

step. Cell imaging was performed using an Olympus IX81 microscope equipped with an UPlanSApo 100x/1.40 oil objective (Olympus Optical, Hamburg, Germany). Digital images were taken with a CoolSNAP HQ2 CCD camera and adjusted for contrast and brightness using the Olympus Soft Imaging Viewer software (Olympus Soft Imaging Solutions GmbH) and MetaMorph 7 (Molecular Devices, USA). Confocal images were obtained using a Zeiss LSM 510 META inverted microscope equipped with a Plan Apochromat 63x/1.4 NA (oil/dic) objective (Carl Zeiss, Oberkochen, Germany), using the Argon 488nm and He 543nm laser lines. Digital images were adjusted for contrast and brightness using the Zeiss LSM Image Browser software (Carl Zeiss MicroImaging GmbH). Live-cell imaging data was collected using an Olympus IX81 microscope equipped with a Yokogawa CSUX1 spinning disk head, CoolSNAP HQ2 CCD camera, 60 x/1.35 oil objective. Digital images were taken and processed using VisiView software (Visitron Systems, Germany). For live-cell imaging, cells were plated in 3.5 cm diameter glass bottom dishes (Cellvis and MatTek). Prior to image acquisition, a controlled temperature chamber was set-up on the microscope stage at 37ºC, as well as an objective warmer. During image acquisition, cells were kept at 37ºC and in CO_2–independent medium (HEPES buffered). For COS-7 cells, 500 stacks of 5 planes (0.5 µm thickness, 100 ms exposure) were taken in a continuous stream. For human fibroblasts, 250 stacks of 9 planes (0.5 µm thickness, 100 ms exposure) were taken in a continuous stream. All conditions and laser intensities were kept between experiments. For each condition analysed, a representative cell was selected and the acquired images were converted into a video at 10x the original speed.

Peroxisome motility, number and length measurements

Peroxisomes were automatically detected and tracked using a customised in-house algorithm [41,46]. Briefly, each image was filtered using a scale-space Laplace of Gaussian filtering approach [58,59] over scales corresponding to the size range of peroxisomes. After filtering, a threshold was determined using the median absolute deviation as a robust estimator of the background level [60], and applied to the filter response to determine peroxisome positions. Once detected, peroxisomes were tracked using a global optimization subroutine (using a modified version of the Jonker-Volgenant algorithm [61]. Tracking results were manually verified for accuracy. For trajectory plots, 100 trajectories were retrieved for each condition by randomly selecting approximately 4 trajectories, of length at least 20 time-frames, from each

dataset. Next the trajectories were re-centred such that each trajectory started at (0,0), and subsequently smoothed applying a simple moving-average algorithm using a Hann window. The first 20 time-frames for these trajectories were then plotted starting at a centre. For CDF plots, basic instantaneous trajectory speed profiles were estimated by calculating the distance moved between each time-point in the trajectory. These speeds were then pooled and converted into an Empirical Cumulative Distribution Function (ECDF). By pooling the speeds for all datasets for a given condition a single ECDF for each condition was generated. Trajectories for the tracked peroxisomes were analysed by splitting their instantaneous speeds into two groups, using a cut-off for linear motion speed of 0.24 μm/s [42]. The relative populations of the two groups of peroxisome speeds were used as an indication of the amount of linear motion for each dataset, and compared against all trajectories to obtain a percentage of microtubule-dependent motility per cell. The number of peroxisomes per cell was obtained from the motility analysis output, and determined by the detected peroxisome from the first frame of each analysed cell. Peroxisome protrusion lengths were obtained from live-cell imaging data and manually measured using MetaMorph 7. Each observed protrusion was measured at the longest point of extension. Kymographs were generated using ImageJ.

Immunoprecipitation

For immunoprecipitation experiments Myc-MIRO1 WT and HA-PEX19 were expressed in COS-7 cells. After 48 h cells were washed in PBS and incubated with 1 mM DSP followed by quenching with 100 mM Tris pH 7.4. After crosslinking cells were lysed in ice-cold lysis buffer (25 mM Tris-HCl pH 7.5, 150 mM NaCl, 0.5% Triton X-100, 1 mM PMSF and protease inhibitor cocktail). Undissolved material was pelleted by centrifugation at 15,000 g. The supernatant was mixed with Myc-antibody coupled agarose beads and incubated for 2 h at 4°C. Beads were subsequently washed extensively with lysis buffer by quick centrifugations at 12,000 g and by incubating in a rotating shaker for 15 minutes at 4ºC. Bound proteins were eluted with 50 mM NaOH and the eluted protein was denatured in Laemmli buffer for 10 minutes at 95ºC. Immunoprecipitates and total lysates were analyzed by Western immunoblotting.

Mathematical modelling

Each PO was described by its body radius r and elongation length L. Simulations were started with 250 PO, each with a random initial radius and no elongation. After each time step (Δt=1s), we implemented three processes. First, lipid flow from the ER into the body: the body surface area was increased by $\alpha\Delta t$ with probability $e^{-\gamma A}$, where A is the total area of all peroxisomes. Second, if the body radius was above r_{min}, the elongation was increased by length $v\Delta t$, with the extra elongation area taken from the body. Third, when the elongation length was longer than L_{min}, peroxisomes underwent division with probability $\beta L\Delta t$. In addition, during each time step, each peroxisome had probability $\Delta t/\tau$ of being removed by turnover. Simulations were carried out in C++ and MATLAB. See Supporting Information for full details.

Statistical analyses

For quantitative analysis of the effect of MIRO1 expression on peroxisome distribution, motility and number, at least 3 independent experiments were carried out. Statistical analyses were performed using Microsoft Excel and GraphPad Prism 5 software. Data are presented as means ± SEM. Two-tailed unpaired t-tests and one-way ANOVA with post hoc Tukey tests were used to determine statistical differences against control values. * $p<0.05$, ** $p<0.01$, *** $p<0.001$.

Acknowledgements

We thank all colleagues who provided cell lines, plasmids and antibodies (see Tables S1-S4). This work was supported by BBSRC (BB/K006231/1, BB/N01541X/1) and FCT (PTDC/BIA-BCM/118605/2010) to MS; DMR, MS and JM were supported by a Wellcome Trust Institutional Strategic Support Award (WT105618MA; WT097835MF) and DMR by the Medical Research Council (MR/P022405/1). DR and AG were supported by personal fellowship grants from the Portuguese Foundation for Science and Technology (FCT) (SFRH/BPD/77619/2011; SFRH/BD/81223/2011) under the scope of “Programa Operacional Temático Factores de Competitividade” (COMPETE) of “Quadro Comunitário de Apoio III” and co-financed by Fundo Comunitário Europeu (FEDER). The authors declare no conflict of interest.

References

1. Schrader M, Costello JL, Godinho LF, Azadi AS, Islinger M. Proliferation and fission of peroxisomes - An update. *Biochim Biophys Acta - Mol Cell Res*. 2016;1863:971-983.

2. Waterham HR, Ferdinandusse S, Wanders RJA. Human disorders of peroxisome metabolism and biogenesis. *Biochim Biophys Acta - Mol Cell Res*. 2016;1863(5):922-933.

3. Nordgren M, Fransen M. Peroxisomal metabolism and oxidative stress. *Biochimie*. 2014;98(1):56-62.

4. Schrader M, Godinho LF, Costello JL, Islinger M. The different facets of organelle interplay—an overview of organelle interactions. *Front Cell Dev Biol*. 2015;3:56.

5. Shai N, Schuldiner M, Zalckvar E. No peroxisome is an island - Peroxisome contact sites. *Biochim Biophys Acta - Mol Cell Res*. 2016;1863(5):1061-1069.

6. Valm AM, Cohen S, Legant WR, et al. Applying systems-level spectral imaging and analysis to reveal the organelle interactome. *Nature*. 2017;546(7656):162-167.

7. Fagarasanu A, Mast FD, Knoblach B, Rachubinski R a. Molecular mechanisms of organelle inheritance: lessons from peroxisomes in yeast. *Nat Rev Mol Cell Biol*. 2010;11(9):644-654.

8. Sparkes I, Gao H. Plant Peroxisome Dynamics: Movement, Positioning and Connections. In: *Molecular Machines Involved in Peroxisome Biogenesis and Maintenance*. Springer; 2014:461-477.

9. Schrader M, Burkhardt JK, Baumgart E, et al. Interaction of microtubules with peroxisomes. Tubular and spherical peroxisomes in HepG2 cells and their alteractions induced by microtubule-active drugs. *Eur J Cell Biol*. 1996;69:24-35.

10. Schrader M, King SJ, Stroh TA, Schroer TA. Real time imaging reveals a peroxisomal reticulum in living cells. *J Cell Sci*. 2000;113:3663-3671.

11. Wiemer EAC, Wenzel T, Deerinck TJ, Ellisman MH, Subramani S. Visualization of the peroxisomal compartment in living mammalian cells: dynamic behavior and association with microtubules. *J Cell Biol*. 1997;136(1):71–80.

12. Rapp S, Saffrich R, Anton M, et al. Microtubule-based peroxisome movement. *J Cell Sci*. 1996;109:837-849.

13. Schrader M, Reuber BE, Morrell JC, et al. Expression of PEX11β mediates peroxisome proliferation in the absence of extracellular stimuli. *J Biol Chem*. 1998;273(45):29607-29614.

14. Delille HK, Agricola B, Guimaraes SC, et al. Pex11pbeta-mediated growth and division of mammalian peroxisomes follows a maturation pathway. *J Cell Sci*. 2010;123(Pt 16):2750-2762.

15. Williams C, Opalinski L, Landgraf C, et al. The membrane remodeling protein Pex11p activates the GTPase Dnm1p during peroxisomal fission. *Proc Natl Acad Sci U S A*. 2015;112(20):6377-6382.

16. Asare A, Levorse J, Fuchs E. Coupling organelle inheritance with mitosis to balance growth and differentiation. *Science*. 2017;355(6324):eaah4701. doi:10.1126/science.aah4701.

17. Schrader M, Fahimi HD. Growth and division of peroxisomes. *Int Rev Cytol*. 2006;255(6):237-290.

18. Chang J, Mast FD, Fagarasanu A, et al. Pex3 peroxisome biogenesis proteins function in peroxisome inheritance as class V myosin receptors. *J Cell Biol*. 2009;187(2):233-246.

19. Otzen M, Rucktäschel R, Thoms S, et al. Pex19p contributes to peroxisome inheritance in the association of peroxisomes to Myo2p. *Traffic*. 2012;13(7):947-959.

20. Dietrich D, Seiler F, Essmann F, Dodt G. Identification of the kinesin KifC3 as a new player for positioning of peroxisomes and other organelles in mammalian cells. *Biochim Biophys Acta - Mol Cell Res*. 2013;1833(12):3013-

3024.

21. Fransson A, Ruusala A, Aspenström P. Atypical Rho GTPases have roles in mitochondrial homeostasis and apoptosis. *J Biol Chem*. 2003;278(8):6495-6502.

22. MacAskill AF, Rinholm JE, Twelvetrees AE, et al. Miro1 is a calcium sensor for glutamate receptor-dependent localization of mitochondria at synapses. *Neuron*. 2009;61(4):541-555.

23. Saotome M, Safiulina D, Szabadkai G, et al. Bidirectional Ca2+ -dependent control of mitochondrial dynamics by the Miro GTPase. *Proc Natl Acad Sci U S A*. 2008;105(52):20728-20733.

24. van Spronsen M, Mikhaylova M, Lipka J, et al. TRAK/Milton Motor-Adaptor Proteins Steer Mitochondrial Trafficking to Axons and Dendrites. *Neuron*. 2013;77(3):485-502.

25. Wang X, Schwarz TL. The Mechanism of Ca2+ -Dependent Regulation of Kinesin-Mediated Mitochondrial Motility. *Cell*. 2009;136(1):163-174.

26. Devine MJ, Birsa N, Kittler JT. Miro sculpts mitochondrial dynamics in neuronal health and disease. *Neurobiol Dis*. 2016;90:27-34.

27. Yamaoka S, Hara-Nishimura I. The mitochondrial Ras-related GTPase Miro: views from inside and outside the metazoan kingdom. *Front Plant Sci*. 2014;5:350.

28. Klosowiak JL, Focia PJ, Chakravarthy S, Landahl EC, Freymann DM, Rice SE. Structural coupling of the EF hand and C-terminal GTPase domains in the mitochondrial protein Miro. *EMBO Rep*. 2013;14(11):968-974.

29. Schuler M-H, Lewandowska A, Caprio G Di, et al. Miro1-mediated mitochondrial positioning shapes intracellular energy gradients required for cell migration. Steinberg G, ed. *Mol Biol Cell*. 2017;28(16):2159-2169.

30. Koch A, Yoon Y, Bonekamp NA, Mcniven MA, Schrader M. A Role for Fis1 in Both Mitochondrial and Peroxisomal Fission in Mammalian Cells. *Mol Biol Cell*. 2005;16:5077-5086.

31. Delille HK, Schrader M. Targeting of hFis1 to peroxisomes is mediated by Pex19p. *J Biol Chem*. 2008;283(45):31107-31115.

32. Gandre-Babbe S, van der Bliek AM. The novel tail-anchored membrane protein Mff controls mitochondrial and peroxisomal fission in mammalian cells. *Mol Biol Cell*. 2008;19:2402-2412.

33. Huber N, Guimaraes SC, Schrader M, Suter U, Niemann A. Charcot-Marie-Tooth disease-associated mutants of GDAP1 dissociate its roles in peroxisomal and mitochondrial fission. *EMBO Rep*. 2013;14(6):545-552.

34. Costello JL, Castro IG, Camoes F, et al. Predicting the targeting of tail-anchored proteins to subcellular compartments in mammalian cells. *J Cell Sci*. 2017;130:1675-1687.

35. Wiese S, Gronemeyer T, Ofman R, et al. Proteomics characterization of mouse kidney peroxisomes by tandem mass spectrometry and protein correlation profiling. *Mol Cell Proteomics*. 2007;6(12):2045–2057.

36. Jadot M, Boonen M, Thirion J, et al. Accounting for Protein Subcellular Localization: A Compartmental Map of the Rat Liver Proteome. *Mol Cell Proteomics*. 2017;16(2):194-212.

37. Huttlin EL, Ting L, Bruckner RJ, et al. The BioPlex Network: A Systematic Exploration of the Human Interactome. *Cell*. 2015;162(2):425-440.

38. Fransson A, Ruusala A, Aspenström P. The atypical Rho GTPases Miro-1 and Miro-2 have essential roles in mitochondrial trafficking. *Biochem Biophys Res Commun*. 2006;344(2):500-510

39. Halbach A, Landgraf C, Lorenzen S, et al. Targeting of the tail-anchored peroxisomal membrane proteins PEX26 and PEX15 occurs through C-terminal PEX19-binding sites. *J Cell Sci*. 2006;119(Pt 12):2508-2517.

40. Lin C, Schuster M, Guimaraes SC, et al. Active diffusion and microtubule-based transport oppose myosin forces to position organelles in cells. *Nat Commun*. 2016;(7):11814.

41. Metz J, Castro IG, Schrader M. Peroxisome Motility Measurement and

Quantification Assay. *Bio-protocol*. 2017;7(17).

42. Bonekamp NA, Sampaio P, de Abreu FV, Lüers GH, Schrader M. Transient Complex Interactions of Mammalian Peroxisomes Without Exchange of Matrix or Membrane Marker Proteins. *Traffic*. 2012;13(7):960-978.

43. Nguyen TT, Oh SS, Weaver D, et al. Loss of Miro1-directed mitochondrial movement results in a novel murine model for neuron disease. *Proc Natl Acad Sci*. 2014;111(35):E3631-3640.

44. Guimaraes SC, Schuster M, Bielska E, et al. Peroxisomes, lipid droplets, and endoplasmic reticulum “hitchhike” on motile early endosomes. *J Cell Biol*. 2015;211(5):945-954.

45. Nguyen T, Bjorkman J, Paton BC, Crane DI. Failure of microtubule-mediated peroxisome division and trafficking in disorders with reduced peroxisome abundance. *J Cell Sci*. 2006;119(Pt 4):636-645.

46. Costello JL, Castro IG, Hacker C, et al. ACBD5 and VAPB mediate membrane associations between peroxisomes and the ER. *J Cell Biol*. 2017;216(2):331-342.

47. Bharti P, Schliebs W, Schievelbusch T, et al. PEX14 is required for microtubule-based peroxisome motility in human cells. *J Cell Sci*. 2011;124(Pt 10):1759-1768.

48. Mathur J, Mammone A, Barton KA. Organelle extensions in plant cells. *J Integr Plant Biol*. 2012;54(11):851-867.

49. Passmore JB, Pinho S, Gomez-Lazaro M, Schrader M. The respiratory chain inhibitor rotenone affects peroxisomal dynamics via its microtubule-destabilising activity. *Histochem Cell Biol*. 2017;148(3):331-341.

50. Santos MJ, Imanaka T, Lazarow PB. Peroxisomal Integral Membrane Proteins in Control and Zellweger Fibroblasts. *J Biol Chem*. 1988;263(21):10502-10509.

51. Itoyama A, Honsho M, Abe Y, Moser A, Yoshida Y, Fujiki Y. Docosahexaenoic acid mediates peroxisomal elongation, a prerequisite for peroxisome division. *J Cell Sci*. 2012;125(Pt 3):589-602.

52. Koch J, Feichtinger RG, Freisinger P, et al. Disturbed mitochondrial and peroxisomal dynamics due to loss of MFF causes Leigh-like encephalopathy, optic atrophy and peripheral neuropathy. *J Med Genet*. 2016;53(4):270-278.

53. Shamseldin HE, Alshammari M, Al-Sheddi T, et al. Genomic analysis of mitochondrial diseases in a consanguineous population reveals novel candidate disease genes. *J Med Genet*. 2012;49(4):234-241.

54. Li X, Gould SJ. PEX11 promotes peroxisome division independently of peroxisome metabolism. *J Cell Biol*. 2002;156(4):643-651.

55. Okumoto K, Ono T, Toyama R, Shimomura A, Nagata A, Fujiki Y. New splicing variants of mitochondrial Rho GTPase-1 (Miro1) transport peroxisomes. *J Cell Biol*. December 2017:jcb.201708122.

56. Hoepfner D, van den Berg M, Philippsen P, Tabak HF, Hettema EH. A role for Vps1p, actin, and the Myo2p motor in peroxisome abundance and inheritance in Saccharomyces cerevisiae. *J Cell Biol*. 2001;155(6):979-990.

57. Nagotu S, Saraya R, Otzen M, Veenhuis M, van der Klei IJ. Peroxisome proliferation in Hansenula polymorpha requires Dnm1p which mediates fission but not de novo formation. *Biochim Biophys Acta*. 2008;1783(5):760-769.

58. Lindeberg T. Feature detection with automatic scale selection. *Int J Comput Vis*. 1998;30(2):79-116.

59. Lindeberg T. *Scale-Space Theory in Computer Vision*. Vol 256. Springer Science & Business Media; 2013.

60. Murtagh F, Starck J-L. Image processing through multiscale analysis and measurement noise modeling. *Stat Comput*. 2000;10(2):95-103.

61. Jonker R, Volgenant A. A shortest augmenting path algorithm for dense and sparse linear assignment problems. *Computing*. 1987;38(4):325-340.

Figure legends

Fig. 1. MIRO1 is targeted to peroxisomes and alters their distribution in COS-7 cells. (**A**) COS-7 cells were transfected with Myc-MIRO1, fixed and stained against Myc, and PEX14 or TOM20. (**B**) Co-immunoprecipitation from COS-7 cells expressing HA-PEX19 and Myc-MIRO1, using α-Myc-conjugated agarose beads. HA-PEX19 only co-immunoprecipitated in the presence of Myc-MIRO1. Higher band in α-Myc Input is unspecific. Input – 10% of total cell lysates, IP – immunoprecipitation. (**C**) Schematic view of MIRO1 domains and mutation sites and the Myc-MIRO1^{PEX} construct. (**D-F**) COS-7 cells were transfected with Myc-MIRO1^{PEX} constructs and stained against Myc and PEX14 or TOM20; (**D**) Myc-MIRO1^{Pex} was exclusively targeted to peroxisomes and induced re-distribution to the cell periphery (**E**) without affecting mitochondrial morphology and distribution; (**F**) Mutated Myc-MIRO1^{Pex} proteins were exclusively targeted to peroxisomes and induced the formation of peroxisomal accumulations in the cell periphery (V13) or scattered (V13, N18 and KK). (**G**) Quantitative analysis of peroxisome distribution in (**D-F**). Cells with peroxisomal accumulations in the periphery or scattered were counted. Values represent mean ± SEM of 3 independent experiments (100 replicates per experiment per condition; ** $p<0.01$; *** $p<0.001$; one-way ANOVA with post hoc Tukey test vs control). Bars, 20 µm (overview), 5 µm (magnification)

Fig. 2. MIRO1 expression increases microtubule-dependent peroxisome motility in mammalian cells and induces peroxisome proliferation in human skin fibroblasts. (**A-C**) Myc-MIRO1$^{V13\text{-}Pex}$ expression increases peroxisome movement. COS-7 cells were transfected with Myc-Miro1$^{V13\text{-}Pex}$ and EGFP-SKL. For each cell, 500 stacks of 5 planes were obtained over time, and peroxisomes detected and tracked using an automated algorithm. (**A**) Trajectory plots. 100 peroxisome trajectories were retrieved for each condition and the first 20 time frames plotted starting at a centre. (**B**) Cumulative distribution function (CDF) plot. Instantaneous trajectory speed profiles were estimated by calculating distance moved between each time point in the trajectory. These speeds were pooled and converted to an empirical cumulative distribution function (ECDF). By pooling speeds for all datasets for a given condition, a single ECDF was generated for each. A threshold of 0.24 µm/s was defined for microtubule-dependent motility. (**C**) Percentage of fast moving peroxisomes per cell in

control and Myc-MIRO1$^{V13\text{-}Pex}$ expressing cells. Values represent mean ± SEM of 20 to 30 cells from 3 independent experiments (*** p<0.001; two-tailed unpaired t-test vs control cells). (**D**) C109, dPEX5 and dPEX14 cells were transfected with Myc-MIRO1^{Pex}, fixed and stained against PEX14, TOM20, PMP70 and Myc. Expression of Myc-MIRO1^{Pex} induces peroxisome proliferation. (**E-F**) C109, dPEX5 and dPEX14 cells were transfected with EGFP-ACBD5$^{TMD\text{-}T}$ (peroxisomal membrane marker) alone, or co-transfected with Myc-MIRO1^{Pex}. For each cell analysed, 250 stacks of 9 planes were obtained over time, and peroxisomes were detected and tracked using an automated algorithm. (**E**) Quantitative analysis of peroxisome number (first stack of each tracked cell). In all cases, expression of Myc-MIRO1^{Pex} significantly increased peroxisome number: C109 – 741 ± 53 vs 1040 ± 101, dPEX5 – 304 ± 27 vs 710 ± 51, and dPEX14 – 268 ± 18 vs 457 ± 58. Values represent mean ± SEM of 24 to 29 cells from 3 independent experiments (* p<0.05; ** p<0.01; *** p<0.001; one-way ANOVA with post hoc Tukey test vs controls). (**F**) Percentage of fast moving peroxisomes per cell in control and Myc-MIRO1^{Pex} expressing fibroblasts. In all cases, peroxisome motility was significantly increased upon MIRO1 expression: C109 – 4.51 ± 0.43 vs 11.05 ± 1.32, dPEX5 – 1.61 ± 0.20 vs 8.25 ± 1.17, dPEX14 – 3.36 ± 0.30 vs 8.30 ± 1.59. Values represent mean ± SEM of 14 to 26 cells in three independent experiments. Bars, 20 µm (overview), 5 µm (magnification)

Fig. 3. Expression of MIRO1 increases the length of peroxisome elongations in dPEX5 patient fibroblasts. (**A-B**) dPEX5 patient fibroblasts were transfected with Myc-MIRO1^{Pex}, fixed and stained against (**A**) Myc and PEX14. The majority of observed elongations in fixed cells show an evenly distributed Myc-MIRO1^{Pex} signal (arrowheads), likely originating from a large peroxisome as shown by the strong PEX14 staining at one of the extremities (arrowheads). (**B**) dPEX5 cells were fixed and stained against PEX14 and TUBULIN. Elongated peroxisomal structures were usually found overlaying microtubules (arrowheads). (**C-E**) dPEX5 patient fibroblasts were transfected with EGFP-ACBD5$^{TMD\text{-}T}$ (peroxisomal membrane marker) and Myc-MIRO1^{Pex} (**C**) Time lapse of peroxisome elongation forming and retracting in a dPEX5 cell expressing EGFP-ACBD5$^{TMD\text{-}T}$ and Myc-MIRO1^{Pex}. (**D**) Kymograph of peroxisome elongation observed in (**C**). Bars, 20 s (vertical), 5 µm (horizontal). (**E**) Quantitative analysis of peroxisome elongation length in dPEX5 and dPEX14 cells. Expression of Myc-MIRO1^{Pex} significantly increased the length of peroxisome elongations in dPEX5

cells (1.62 ± 0.08 vs 2.21 ± 0.15), but not in dPEX14 cells (1.44 ± 0.07 vs 1.47 ± 0.09). Values represent mean ± SEM from 22 to 29 cells, 3 independent experiments (*** p<0.001; two-tailed unpaired t-test vs controls). Bars, 20 µm (overview), 5 µm (magnification)

Fig. 4. (A) Mathematical model of peroxisomal growth and division. (a) Each peroxisome is represented as a spherical body of radius *r* and a cylindrical elongation of length *L* and diameter *w* (b) The three processes implemented in the model: (i) membrane lipid flow into the body with rate α and lipid flow constant γ, (ii) growth of the elongation at speed *v*, and (iii) division with rate per unit length β. (c) Snapshot from the model simulation of wild-type cells (α=75nm^2/s, β=2x10^{-5}/nm/s, *v*=0.3nm/s, τ=40hrs, γ=2.4x10^{-7}nm^{-2}). (d) Snapshot from the simulation of dMff cells (with reduced division rate β=5x10^{-11}/nm/s). (e) Snapshot from the simulation of dPex5 cells (β=10^{-9}/nm/s, v=2x10^{-4}nm/s). (f) Snapshot from overexpression of MIRO1 in dPex5 cells (β=10^{-9}/nm/s, v=3nm/s, γ=1.2x10^{-7}nm^{-2}). Bar, 1µm. (**B**) **Schematic representation of the effects of MIRO1 on peroxisome dynamics and morphology**. (a) Un-tethered peroxisomes move via the microtubule cytoskeleton in a MIRO1 dependent manner; (b) Peroxisomes tethered to the ER are pulled by MIRO1-mediated motor forces and divide to form new peroxisomes; (c) Defects in peroxisomal metabolism compromise MIRO1-mediated peroxisome division and proliferation resulting in elongated membrane protrusions.

Fig. 5. PEX11β promotes peroxisome membrane elongation and division. (**A**) PEX5 deficient patient fibroblasts or (**B-C**) COS-7 cells were transfected with PEX11β-EGFP. (**A**) PEX11β-EGFP induces peroxisome proliferation, leading to the formation of elongated peroxisomes (top), followed by their fission into numerous small peroxisomes (bottom). (**C**) Time lapse of peroxisome elongation (left) and division (right). Note the directed, long-range movement of a peroxisome (arrow) with the linear protrusion leading (28-40s). The same peroxisome becomes static, whereas the membrane protrusion exhibits a more random, tentacle-like movement (42-54s) before it divides (135-141s) (circles) (see also Suppl. Video S10). For each cell analysed, 200 stacks of 9 planes were obtained over time. Time in seconds. Bars, 20 µm (overview), 5 µm (magnification).

Supplemental Figure Legends

Suppl. Fig. S1. (**A**) COS-7 cells transfected with Myc-MIRO1 wild-type and mutants were fixed and stained against Myc and PEX14. Expressed Myc-MIRO1 localizes to peroxisomes and mitochondria, and alters their distribution. All of the expressed mutants show peroxisomal (and mitochondrial) localisation, except for Myc-MIRO1$^{\Delta TM}$, which is cytosolic. Bars, 20 µm (overview), 5 µm (magnification). (**B**) Quantitative analysis of peroxisome distribution in controls and cells expressing different Myc-MIRO1 plasmids. Cells with peroxisomal accumulations in the periphery or scattered were counted. Values represent mean ± SEM of 3 independent experiments (100 replicates per experiment per condition; ** $p<0.01$; *** $p<0.001$; one-way ANOVA with post hoc Tukey test vs control cells).

Suppl. Fig. S2. (**A**) COS-7 cells were transfected with Myc-MIRO1^{Pex} and, after 24 hours, treated with 10 µM nocodazole or DMSO (control) for 4 hours. Fixed cells were stained against Myc and TUBULIN. Cells expressing Myc-MIRO1^{Pex} no longer showed peroxisome aggregates at the cell periphery after treatment with nocodazole. Note that microtubule depolymerisation can lead to peroxisomal aggregates in the cytoplasm. (**B**) Immunoblot of cell lysates from MIRO1 KO and control mouse embryonic fibroblasts (MEFs) stained against MIRO1 and γ-TUBULIN. (**C**) Control and MIRO KO MEFs were transfected with EGFP-SKL and fixed after 24 hours. Bars, 20 µm. (**D**) Control and MIRO1 KO MEFs were transfected with EGFP-SKL. For each cell analysed, 250 stacks of 9 planes were obtained over time. Percentage of fast moving peroxisomes per cell in control (5.54 ± 0.95) and MIRO1 KO cells (5.28 ± 0.93). Values represent mean ± SEM of 8 to 12 cells in 1 experiment. (**E-H**) Cumulative distribution function (CDF) plot. Instantaneous trajectory speed profiles were estimated by calculating the distance moved between each time point in the trajectory. These speeds were pooled and converted to an empirical cumulative distribution function (ECDF). By pooling speeds for all datasets for a given condition, a single ECDF was generated for each. A threshold of 0.24 µm/s was defined for microtubule-dependent motility. (**E**) Control and MIRO1 KO MEFs, (**F**) C109 fibroblasts, (**G**) dPEX5 fibroblasts, (**H**) dPEX14 fibroblasts.

Supplemental Videos

For all videos, cells were analysed by live-cell imaging using an IX81 microscope (Olympus) equipped with a CSUX1 spinning disk head (Yokogawa). 500 stacks of 5 planes (0.5 µm thickness, 100 ms exposure) for COS-7 cells (unless stated otherwise), and 250 stacks of 9 planes for fibroblasts, were taken in a continuous stream.

Videos S1-8 are associated to Figure 2 and Figure S2; Video S9 is associated to Figure 3; Video S10 is associated to Figure 5.

Video S1 – Myc-MIRO1$^{V13\text{-}Pex}$ expression increases peroxisome movement (Control). COS-7 cell transfected with EGFP-SKL. 250 frames, 10× speed.

Video S2 – Myc-MIRO1$^{V13\text{-}Pex}$ expression increases peroxisome movement (Myc-MIRO1$^{V13\text{-}Pex}$). COS-7 cell transfected with EGFP-SKL and Myc-MIRO1$^{V13\text{-}Pex}$. 250 frames, 10× speed.

Video S3 – Myc-MIRO1^{Pex} expression increases peroxisome number and motitlity in human fibroblasts (Control). C109 cell transfected with EGFP-ACBD5$^{TMD\text{-}T}$. 125 frames, 10× speed.

Video S4 – Myc-MIRO1^{Pex} expression increases peroxisome number and motility in human fibroblasts (Myc-MIRO1^{Pex}). C109 cell transfected with EGFP-ACBD5$^{TMD\text{-}T}$ and Myc-MIRO1^{Pex}. 125 frames, 10× speed.

Video S5 – Myc-MIRO1^{Pex} expression increases peroxisome number and motility in human fibroblasts (Control). dPEX5 cell transfected with EGFP-ACBD5$^{TMD\text{-}T}$. 125 frames, 10× speed.

Video S6 – Myc-MIRO1^{Pex} expression increases peroxisome number and motility in human fibroblasts (Myc-MIRO1^{Pex}). dPEX5 cell transfected with EGFP-ACBD5$^{TMD\text{-}T}$ and Myc-MIRO1^{Pex}. 250 frames, 10× speed.

Video S7 – Myc-MIRO1^{Pex} expression increases peroxisome number and motility in human fibroblasts (Control). dPEX14 cell transfected with EGFP-ACBD5$^{TMD\text{-}T}$. 125 frames, 10× speed.

Video S8 – Myc-MIRO1^{Pex} expression increases peroxisome number and motility in human fibroblasts (Myc-MIRO1^{Pex}). dPEX14 cells were transfected with EGFP-ACBD5^{TMD-T} and Myc-MIRO1^{Pex}. 125 frames, 10× speed.

Video S9 – Myc-MIRO1^{Pex} expression induces the formation of peroxisome elongations in dPEX5 patient fibroblasts (cut-out of video S6). dPEX5 cell transfected with EGFP-ACBD5^{TMD-T} and Myc-MIRO1^{Pex}. 160 frames, 10× speed.

Video S10 – PEX11β-EGFP induces peroxisome elongation and proliferation in COS-7 cells. COS-7 cell transfected with PEX11β-EGFP. 200 stacks of 9 planes (0.5 µm thickness, 100 ms exposure) were taken in a continuous stream. 200 frames, 10× speed.

Table S1. **Plasmids used in this study**

Plasmid	Source
EGFP-ACBD5^{TMD-T} WT	[34]
EGFP-SKL	[30]
HA-Pex19	[31]
Myc-MIRO1-WT, V13, N18, KK, ΔTM	P. Aspenström, Karolinska Institute, Sweden
pAH26	R. Erdmann, Univ. Bochum, Germany
PEX11β-EGFP	G. Dodt, Univ. of Tuebingen, Germany

Table S2. **Plasmids generated in this study**

Name	Template	Primers	Enzymes	Vector
Myc-MIRO1-Pex	Myc-Miro1	Myc-Miro1_AgeI_F Miro1_dTM_R	AgeI BglII	pAH26

Table S3. **Primers used in this study**

Name	Sequence (5' to 3')
Myc-Miro1_AgeI_F	GGAACCGGTCACCATGGAGCAGAAGCTGATC
Miro1-dTM_R	GGAAGATCTAAACGTGGAGCTCTTGGGGTC
Miro1seqmid1	CGCACAGAAAGCTGTTCTTCATCC
Miro1seqmid2	GACTGAGCAAGAGTCTCAAG

Table S4. **Primary and secondary antibodies used in this study**

Antibodies	Type	Dilution		Source
		IMF	WB	
HA	mc ms	-	1:1000	BioLegend
MIRO1 (PSI-8027)	pc rb	1:100	1:1000	ProSci
Myc (Ab9106)	mc rb	1:200	1:1000	Abcam
Myc 9E10	mc ms	1:200	1:1000	Santa Cruz Biotechonology
PEX14	pc rb	1:1400	1:4000	D.Crane, Griffith University, Australia
PMP70	mc ms	1:500	1:5000	Sigma-Aldrich
TOM20 (612278)	mc ms	1:200	-	BD Transduction Laboratories
γ-TUBULIN	mc ms	1:100	-	Sigma-Aldrich
AlexaFluor 488 IgG	dk anti-rb	1:500	-	ThermoFisher Scientific
AlexaFluor 488 IgG	dk anti-ms	1:500	-	ThermoFisher Scientific
AlexaFluor 594 IgG	dk anti-rb	1:1000	-	ThermoFisher Scientific
AlexaFluor 594 IgG	dk anti-ms	1:1000	-	ThermoFisher Scientific
HRP IgG	gt anti-ms	-	1:5000	Bio-Rad
HRP IgG	gt anti-rb	-	1:5000	Bio-Rad

Abbreviations: IMF, immunofluorescence; WB, western blot; mc, monoclonal; pc, polyclonal; ms, mouse; rb, rabbit; gt, goat; dk, donkey; HRP, horseradish peroxidase.

Supporting Text for *A role for MIRO1 in motility and membrane dynamics of peroxisomes*

1 Details of mathematical model

Our model describes the shape and number of peroxisomes within a cell. It is a stochastic, population-based model that considers the morphology of a group of peroxisomes, each of which can grow, divide and turnover. Since our aim is to understand the basic biophysical mechanisms involved in peroxisome growth and proliferation, we focus on the peroxisome shape and ignore both their spatial distribution and interactions between each other. Further, we only include a few key processes that affect peroxisome size and number (such as lipid flow and division). This is a deliberate decision that aims to tease out the main factors responsible for peroxisome morphology.

Although we acknowledge that real peroxisome dynamics is likely to be considerably more complex than this, we believe that simpler models with fewer parameters are more valuable and predictive, especially as this is, as far as we know, the first model describing peroxisome shape. The intention is that later models will be able to build on the work described here by including other relevant aspects (such as spatial distribution and interaction).

1.1 Description of model

We describe each peroxisome as consisting of a spherical body of radius r, with the centre at some position $\vec{x}$. In addition, each peroxisome has an optional elongation of length L, emanating at some fixed angle from the body. This elongation is assumed to be straight and to have constant diameter w, so that it can be modelled as a cylinder with a hemispherical cap. Although it is clear that not all real peroxisomes can be described by such a body-elongation arrangement, and although real elongations often bend and have variable width, this idealised representation is sufficient for our present purposes.

We consider three processes by which peroxisomes can change shape: membrane lipid flow, elongation growth, and division. Firstly, peroxisomes are assumed to grow due to membrane lipids flowing from the ER via membrane contacts [1]. Since there is not unlimited lipid, this process is not always successful. To model this we assume that, at any given time, there is some probability $p = e^{-\gamma A}$ that lipid flow occurs, where A is the total surface area of all peroxisomes and γ a constant that we call the lipid flow constant. This means that, in our model, lipid flow is always possible but is less likely

as the total peroxisomal content increases. This assumption that lipid flow depends only on total peroxisome area is simplistic but sufficient for a first model. A more complex model could take account of the spatial distribution of peroxisomes relative to the ER and to *de novo* lipid production. Although lipid flow is unlikely to be constant in practice, we assume for simplicity that there is some fixed rate α at which membrane area tries to flow into the peroxisome. Since peroxisomes without elongations still grow, it is likely that the link to the ER is located somewhere within the body and so we assume that lipid flow only increases the radius of the body without changing the elongation length. Thus, in some time t, the effect of successful lipid flow is to increase r to $\sqrt{r^2 + \alpha t/(4\pi)}$ whilst leaving L unchanged.

Secondly, we consider growth of the elongation. New peroxisomes initially have no elongation ($L = 0$) and must wait until the body radius is above some minimum size $r_{\min}$ before the elongation forms. However, once formed, whenever the body radius is above $r_{\min}$, the elongation then extends at fixed speed v. At the moment a new elongation appears, it consists only of a hemispherical cap of radius $w/2$, which replaces a spherical cap on the body of base radius $w/2$. The membrane area to create this cap is assumed to come from the body, so that r decreases to $\sqrt{r^2 - w^2/8 + \frac{1}{2}r^2(1 - \sqrt{1 - w^2/4r^2})}$ at the moment of formation. Here, the second term corresponds to the surface area of the hemispherical cap and the third term to the surface area of the removed spherical cap ($A_{\text{spherical cap}} = 2\pi rh$, where h is the cap height). The exact mechanism of extension, such as Pex11β oligomerisation or MIRO1-driven motion along microtubules, need not be explicitly specified: from a modelling perspective these mechanisms only differ in the value of v. A more realistic model could consider a variable speed of extension, but this is unlikely to play an important role here. The membrane area required in order to extend the elongation is assumed to come from the body so that the overall membrane area is conserved during the extension process. This means that, after extending for time t, the elongation increases in length to $L + vt$ with a compensating reduction in body size from r to $\sqrt{r^2 - wvt/4}$. The second term originates from the new surface area (πwvt) of the cylindrical elongation.

Thirdly, we include peroxisome division, which occurs by the elongation splitting off to form new peroxisomes. We assume that this can only occur if the elongation length L is above some minimum value $L_{\min}$. We further assume that peroxisomes with longer elongations are more likely to divide, which we implement via a fixed rate of division per unit length, β. We interpret this in a probabilistic manner so that in a small time dt the probability of division is $\beta L dt$. Upon division, the elongation is separated from

the body, split into regularly-sized compartments of length λ, with each becoming a new "daughter" peroxisome. The body of the original peroxisome remains as the "mother" peroxisome. The small cylinder that forms each "daughter" becomes the body of the new peroxisome (with membrane area conserved). After division the "mother" and all "daughter" peroxisomes are without elongations ($L = 0$) and must wait until $r \geq r_{\min}$ before new elongations can form.

In addition, to avoid the number of peroxisomes increasing without limit, we include peroxisome turnover by introducing a mean lifetime τ for each peroxisome. This is implemented as a probability $p = dt/\tau$ that any given peroxisome degrades in a time dt. Finally, the position $\vec{x}$ and elongation angle of each peroxisome undergo diffusion. This is not a crucial part of the current model and is included mainly to improve visualisation of the results. Here we are chiefly interested in the shape of peroxisomes rather than their spatial position. We leave the important issue of spatial distribution for future models.

1.2 Numerical simulation

Each simulation starts with $n = 250$ peroxisomes, with each having a random initial radius and position, and no elongation ($L = 0$). The initial radius is chosen from a truncated normal distribution with mean 70nm, standard deviation 30nm, minimum 40nm and maximum 100nm. At each time step ($\Delta t = 1$s) we implement the three processes described above: (i) r is increased due to membrane lipid flow with probability $e^{-\gamma A}$, (ii) L is increased and r decreased due to elongation growth (for those peroxisomes that are sufficiently large), and (iii) there is a random chance of division (for those peroxisomes with sufficiently long elongations). Further, each peroxisome has probability $\Delta t/\tau$ of undergoing turnover during each time step. The simulation is run for at most 10 days and is stopped once an approximate steady state has been reached (characterised by sufficiently small variations in n, $\langle r \rangle$ and $\langle L \rangle$ over the last six hours).

1.3 Parameter values

At any given time we expect a population of peroxisomes of various sizes and shapes. In particular, at steady state, let n be the number of peroxisomes, f the fraction of peroxisomes that have elongations, $\langle r \rangle$ the average body radius, and $\langle L \rangle$ the average elongation length of those peroxisomes with elongations (*i.e.* of those peroxisomes with $L > 0$). From EM and IMF images of wild-type cells, we estimated that $n \sim 250$, $f \sim 0.1$, $\langle r \rangle \sim 80$nm

and $\langle L \rangle \sim 40$nm. Although these values are likely to vary between different cell types and organisms, they are sufficient for our purpose here, an initial model that sheds light on the biophysical processes involved and recapitulates various mutant phenotypes.

The following sections describe how the wild-type model parameters were estimated. Note that, although it may be possible to find parameters that better fit the data, the fact that (i) these parameters lead to a good match with the wild type, (ii) the model can incorporate overexpression of MIRO1, and (iii) changing only one or two parameters can capture the MFF and PEX5 deficient phenotypes, suggests that this parameter set is sufficient for this first generation model.

1.3.1 The elongation diameter w and compartment length λ

Firstly, from EM images, we measured the average elongation diameter to be about $w = 80$nm [1, 2]. Then, since the smallest new peroxisomes have initial radius $\sqrt{w\lambda/4}$ and since we rarely see peroxisomes smaller than 40nm, this suggests $\lambda \sim 80$nm.

1.3.2 The minimum elongation length for division $L_{\min}$

Next, assuming that most peroxisomes divide very soon after L reaches $L_{\min}$ (which is appropriate for the wild type), the average elongation length $\langle L \rangle \approx \frac{1}{2} L_{\min}$. (This is only approximately true since turnover means that peroxisomes with longer elongations are rarer than those with shorter elongations.) This motivates setting $L_{\min} = 80$nm. Coincidentally, this means that $L_{\min} = \lambda$, which makes sense since then new peroxisomes smaller than 40nm in radius cannot be formed.

1.3.3 The minimum radius for elongation extension $r_{\min}$

By assuming that, for elongating peroxisomes, all available lipid flowing into the body is always used only for elongation growth (*i.e.* $\pi w v > \alpha$), the average body radius can be estimated as $\langle r \rangle \sim (1-f)(\sqrt{w\lambda/4} + r_{\min})/2 + f r_{\min} = \frac{1}{4}(1-f)\sqrt{w\lambda} + \frac{1}{2}(1+f) r_{\min}$. Again, this is only an approximation since the distribution of peroxisome body sizes is not uniform. Using an $\langle r \rangle$ of 80nm then leads to $r_{\min} \sim 110$nm.

1.3.4 The peroxisome mean lifetime τ

Next, to estimate τ, consider overall lipid flow. In steady state, during some time Δt, the total lipid entering the system must exactly balance the lipid

leaving the system. Since the total lipid area entering (due to lipid flow into the body) is approximately $n \cdot \exp(-\gamma n \langle A \rangle) \cdot \alpha \Delta t$, and since the total leaving (due to turnover) is approximately $n \cdot \frac{\Delta t}{\tau} \cdot \langle A \rangle$, we find that $\langle A \rangle = \alpha \tau \exp(-\gamma n \langle A \rangle)$. Then the time between a new peroxisome forming and first starting to elongate, $\pi(4r_{\min}^2 - w\lambda)/(\alpha \exp(-\gamma n \langle A \rangle))$, can be rewritten as $\pi\tau(4r_{\min}^2 - w\lambda)/\langle A \rangle$. Taking a value of 3 days for this, and estimating $\langle A \rangle$ as $4\pi\langle r \rangle^2 + f\pi w \langle L \rangle \approx 10^5 \text{nm}^2$, we conclude that $\tau \sim 1.5 \times 10^5 \text{s}$. This corresponds to a mean peroxisome lifetime of just under 2 days, which agrees well with previously measured values [3].

1.3.5 The division rate β

Given that, at least in the wild type, peroxisomes divide before the elongation length is much greater than $L_{\min}$, a peroxisome that reaches $L_{\min}$ will wait on average about $1/(\beta L_{\min})$ before division. The lack of significant peroxisome elongations in wild-type cells suggests this time is quite short. Taking a value of 10 mins for this, we estimate that $\beta = 2 \times 10^{-5}/\text{nm/s}$.

1.3.6 The lipid flow rate α and lipid flow constant γ

By considering only steady-state values, such as n, f, $\langle r \rangle$ and $\langle L \rangle$, it is not possible to uniquely fit α and γ. This is because these parameters effectively only ever appear together in the combination $\alpha \exp(-\gamma n \langle A \rangle)$, which is the maximum possible lipid flow rate multiplied by the probability of lipid flow actually occurring, and can be thought of as the "effective lipid flow rate". However, it is possible to fit one of these parameters by considering the transient period before steady state. With all other parameters fixed, the time to reach steady state varies inversely with α: smaller/larger values of α take longer/shorter to reach steady state. With the above parameters, our simulations show that choosing $\alpha = 75\text{nm}^2/\text{s}$ means that steady state is reached in a few tens of hours. Once α is fixed, the lipid flow constant γ follows from the overall-lipid-flow equation derived in §1.3.4, which gives $\gamma = \ln(\alpha\tau/\langle A \rangle)/(n\langle A \rangle) \sim 2.4 \times 10^{-7}\text{nm}^{-2}$.

1.3.7 The elongation extension speed v

Finally, we choose the elongation extension speed v so that elongation growth normally uses all the lipid flowing into the body. At steady state, this means that $\pi w v > \alpha \exp(-\gamma n \langle A \rangle)$. In fact, our simulations suggest that a value of $v \sim 0.3\text{nm/s}$ gives a good match to the experimental data for the wild-type and the MFF and PEX5 deficient cases.

1.3.8 Summary

The following table lists all model parameters and their wild-type values.

Parameter	Wild-type value	Section
Lipid flow rate, α	$75\,\mathrm{nm}^2/\mathrm{s}$	§1.3.6
Elongation extension speed, v	$0.3\,\mathrm{nm/s}$	§1.3.7
Division rate, β	$2 \times 10^{-5}\,/\mathrm{nm/s}$	§1.3.5
Peroxisome mean lifetime, τ	$1.5 \times 10^5\,\mathrm{s}$	§1.3.4
Lipid flow constant, γ	$2.4 \times 10^{-7}\,\mathrm{nm}^{-2}$	§1.3.6
Elongation diameter, w	$80\,\mathrm{nm}$	§1.3.1
Elongation comp. length, λ (sets new PO size)	$80\,\mathrm{nm}$	§1.3.1
Minimum r for elongation extension, $r_{\min}$	$110\,\mathrm{nm}$	§1.3.3
Minimum L for division, $L_{\min}$	$80\,\mathrm{nm}$	§1.3.2

References

[1] Costello JL, Castro IG, Hacker C, Schrader TA, Metz J, Zeuschner D, Azadi AS, Godinho LF, Costina V, Findeisen P, Manner A, Islinger M, Schrader M (2017) ACBD5 and VAPB mediate membrane associations between peroxisomes and the ER. *J Cell Biol* 216(2):331–342.

[2] Delille HB, Agricola S, Guimaraes S, Borta H, Luers GH, Fransen M, Schrader M (2010) Pex11pβ-mediated growth and division of mammalian peroxisomes follows a maturation pathway. *J Cell Sci* 123(16):2750–62.

[3] Huybrechts SJ, Van Veldhoven PP, Brees C, Mannaerts GP, Los GV, Fransen M (2009) Peroxisome dynamics in cultured mammalian cells. *Traffic* 10(11):1722–33.

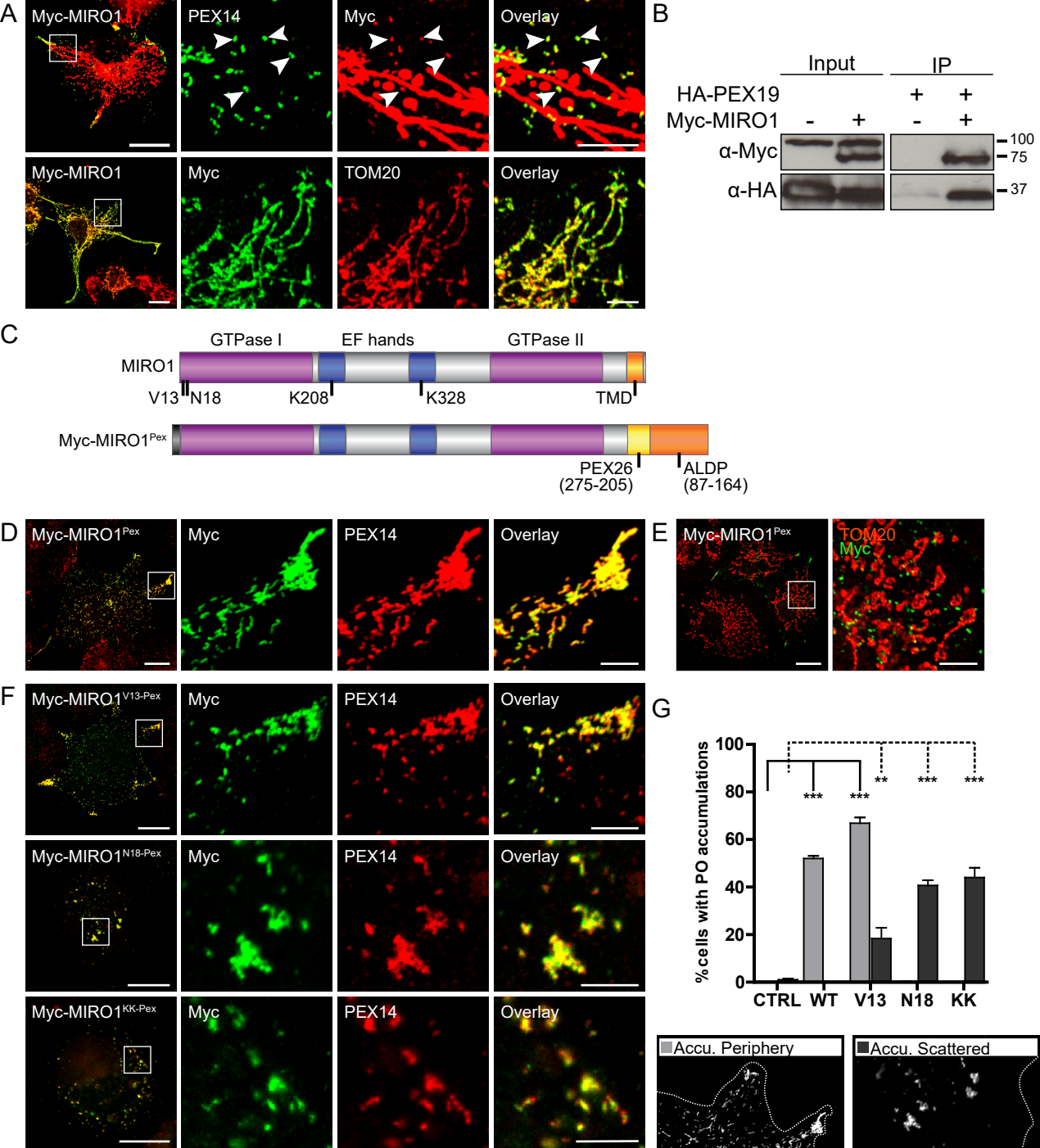
A
Myc-MIRO1
PEX14
Myc
Overlay
Myc-MIRO1
Myc
TOM20
Overlay
B
Input
IP
HA-PEX19
+
+
Myc-MIRO1
-
+
-
+
α-Myc
α-HA
100
75
37
C
GTPase I
EF hands
GTPase II
MIRO1
V13
N18
K208
K328
TMD
Myc-MIRO1Pex
PEX26
(275-205)
ALDP
(87-164)
D
Myc-MIRO1Pex
Myc
PEX14
Overlay
E
Myc-MIRO1Pex
TOM20
Myc
F
Myc-MIRO1V13-Pex
Myc-MIRO1N18-Pex
Myc-MIRO1KK-Pex
Myc
PEX14
Overlay
G
%cells with PO accumulations
100
80
60
40
20
0
***
***
**
***
***
CTRL
WT
V13
N18
KK
Accu. Periphery
Accu. Scattered

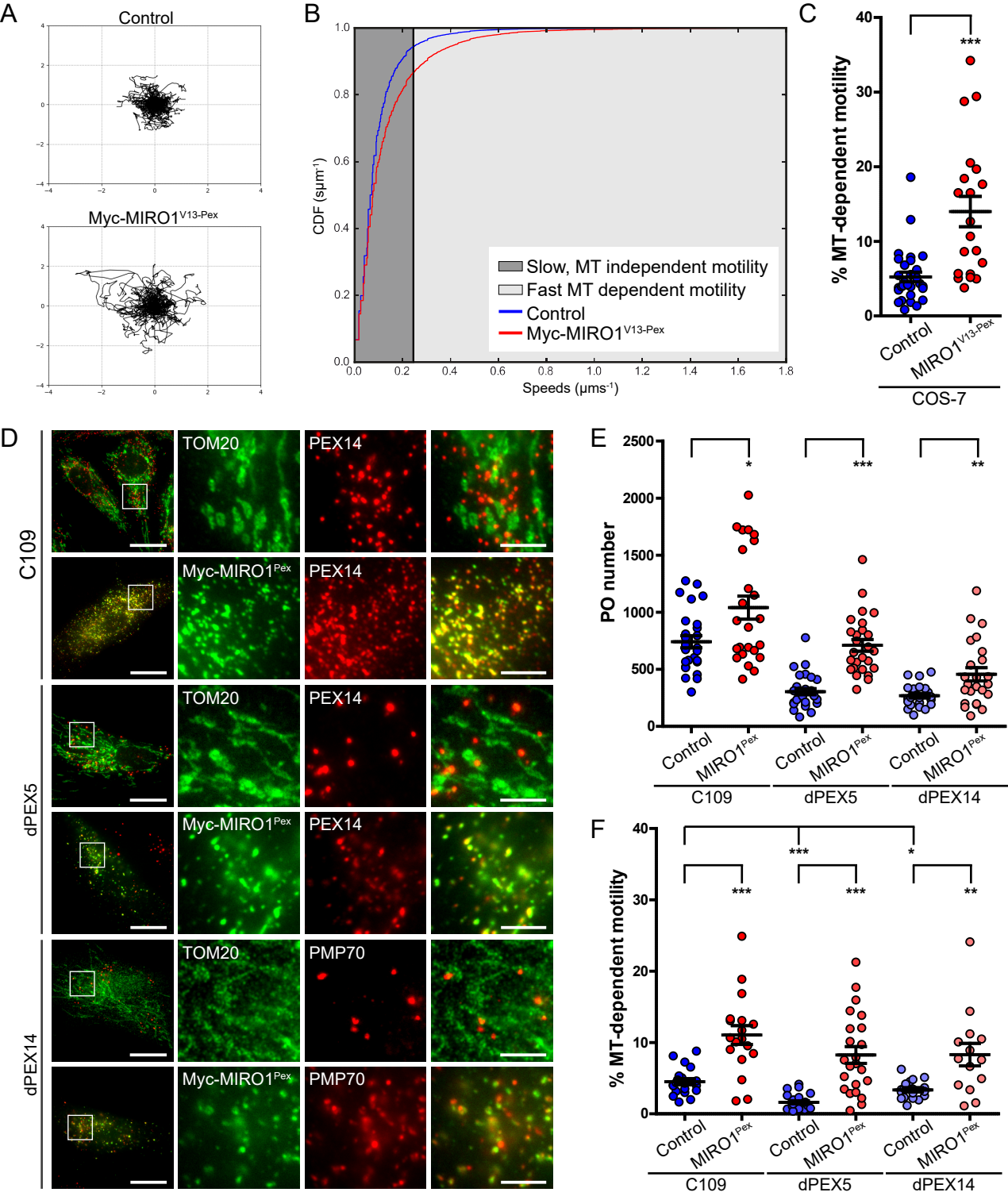
A
Control
Myc-MIRO1V13-Pex
B
CDF (sμm-1)
Speeds (μms-1)
Slow, MT independent motility
Fast MT dependent motility
Control
Myc-MIRO1V13-Pex
C
% MT-dependent motility
Control
MIRO1V13-Pex
COS-7
D
C109
dPEX5
dPEX14
TOM20
PEX14
Myc-MIRO1Pex
PMP70
E
PO number
Control
MIRO1Pex
C109
dPEX5
dPEX14
F
% MT-dependent motility
Control
MIRO1Pex
C109
dPEX5
dPEX14

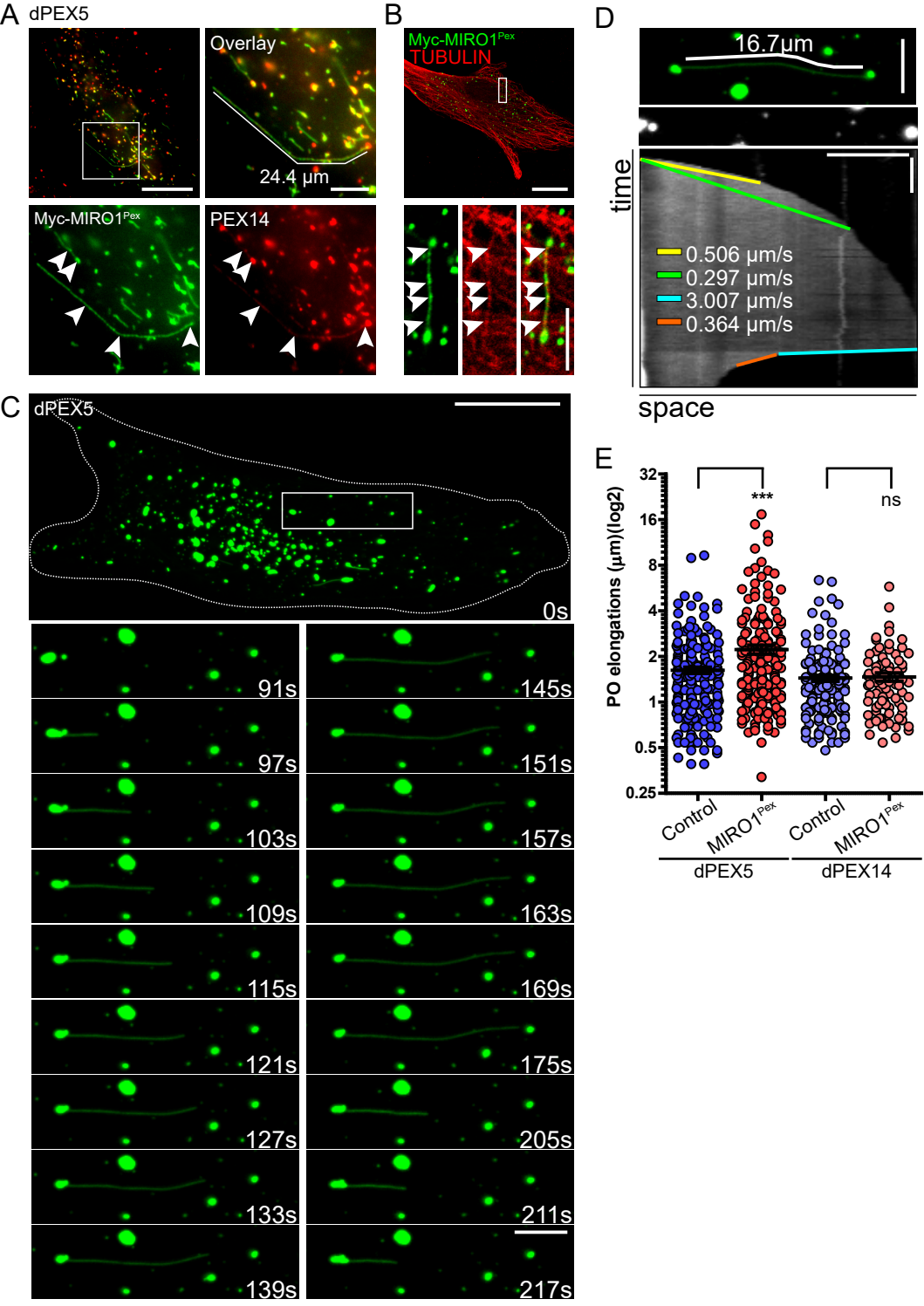
A
dPEX5
Overlay
24.4 µm
Myc-MIRO1Pex
PEX14
B
Myc-MIRO1Pex
TUBULIN
C
dPEX5
0s
91s
97s
103s
109s
115s
121s
127s
133s
139s
145s
151s
157s
163s
169s
175s
205s
211s
217s
D
16.7µm
time
space
0.506 µm/s
0.297 µm/s
3.007 µm/s
0.364 µm/s
E
PO elongations (µm)(log2)
32
16
8
4
2
1
0.5
0.25
***
ns
Control
MIRO1Pex
Control
MIRO1Pex
dPEX5
dPEX14

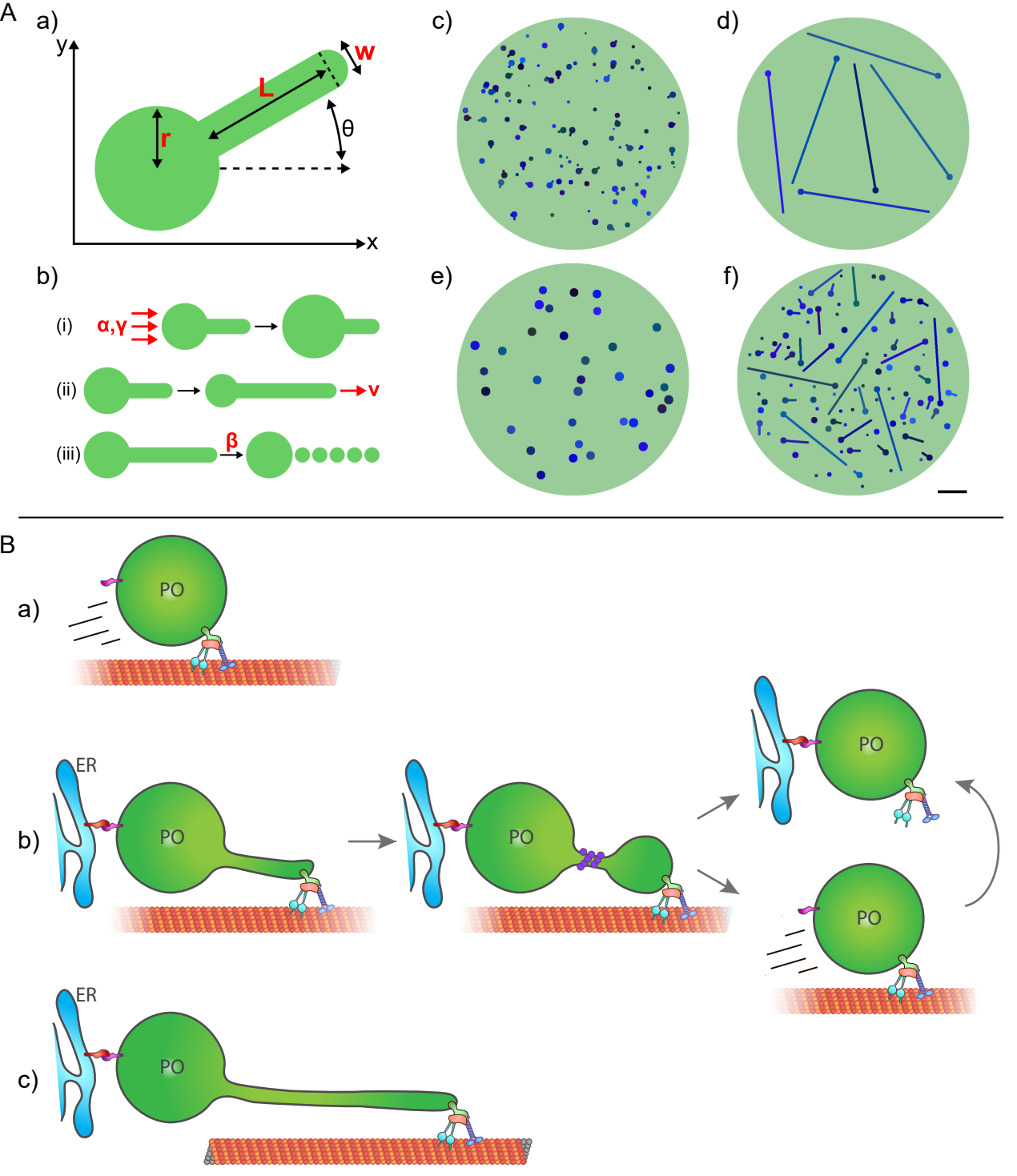
A
a)
y
x
w
L
r
θ
b)
(i)
α,γ
(ii)
v
(iii)
β
c)
d)
e)
f)
B
a)
PO
b)
ER
PO
c)
ER
PO

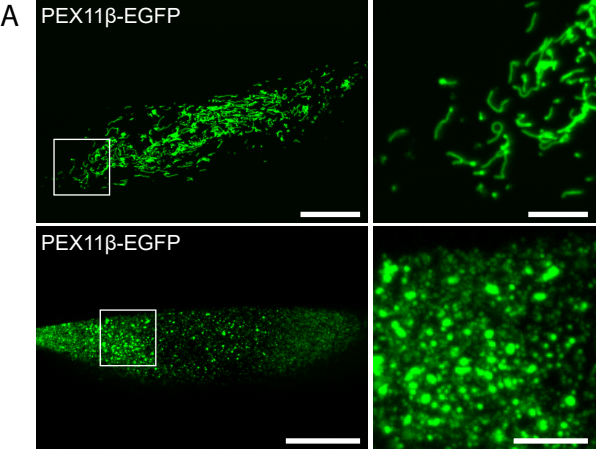
A
PEX11β-EGFP
PEX11β-EGFP

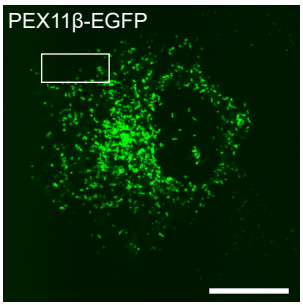
B
PEX11β-EGFP

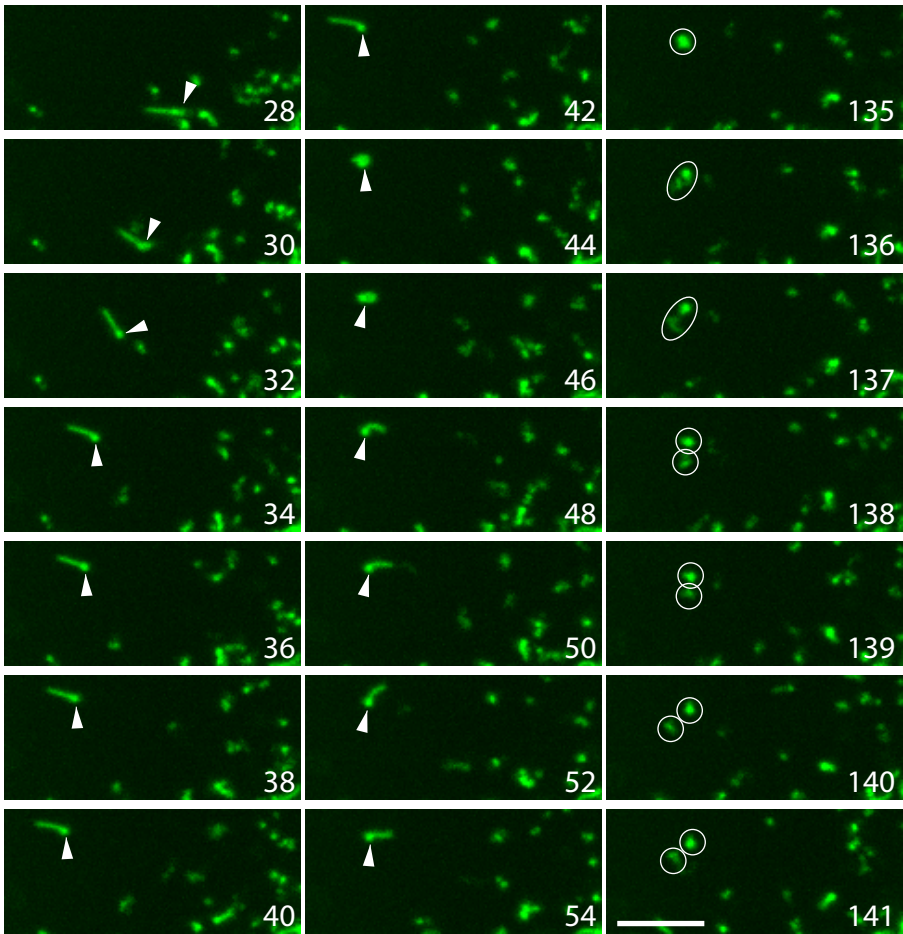
C
28
42
135
30
44
136
32
46
137
34
48
138
36
50
139
38
52
140
40
54
141

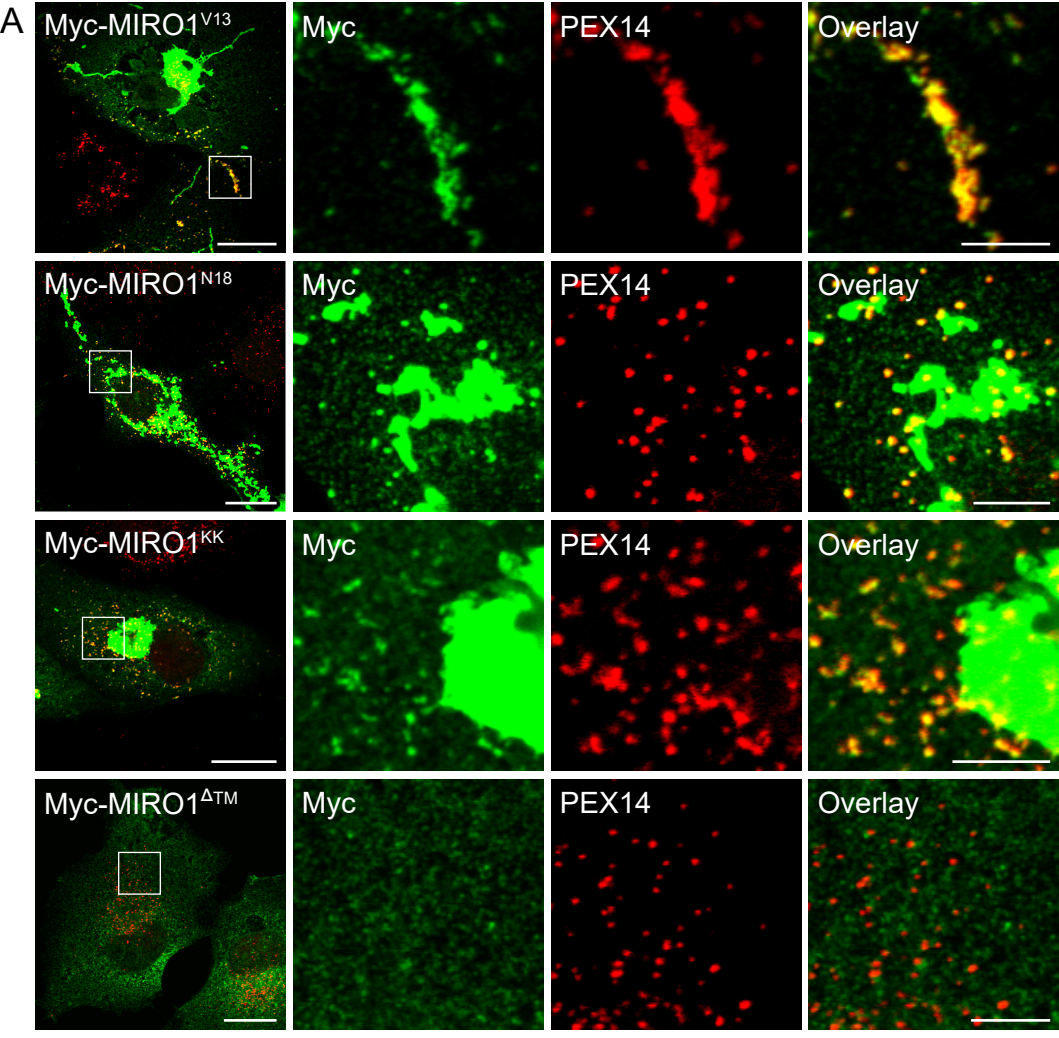
A
Myc-MIRO1V13
Myc
PEX14
Overlay
Myc-MIRO1N18
Myc
PEX14
Overlay
Myc-MIRO1KK
Myc
PEX14
Overlay
Myc-MIRO1ΔTM
Myc
PEX14
Overlay

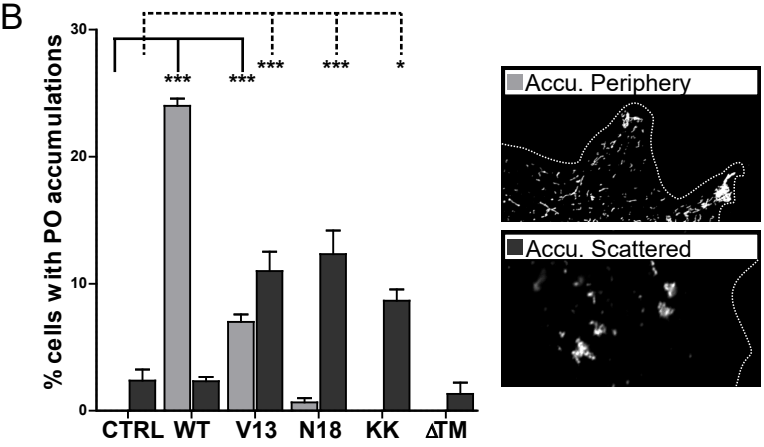
B
% cells with PO accumulations
30
20
10
0
***
***
***
***
*
CTRL
WT
V13
N18
KK
ΔTM
Accu. Periphery
Accu. Scattered

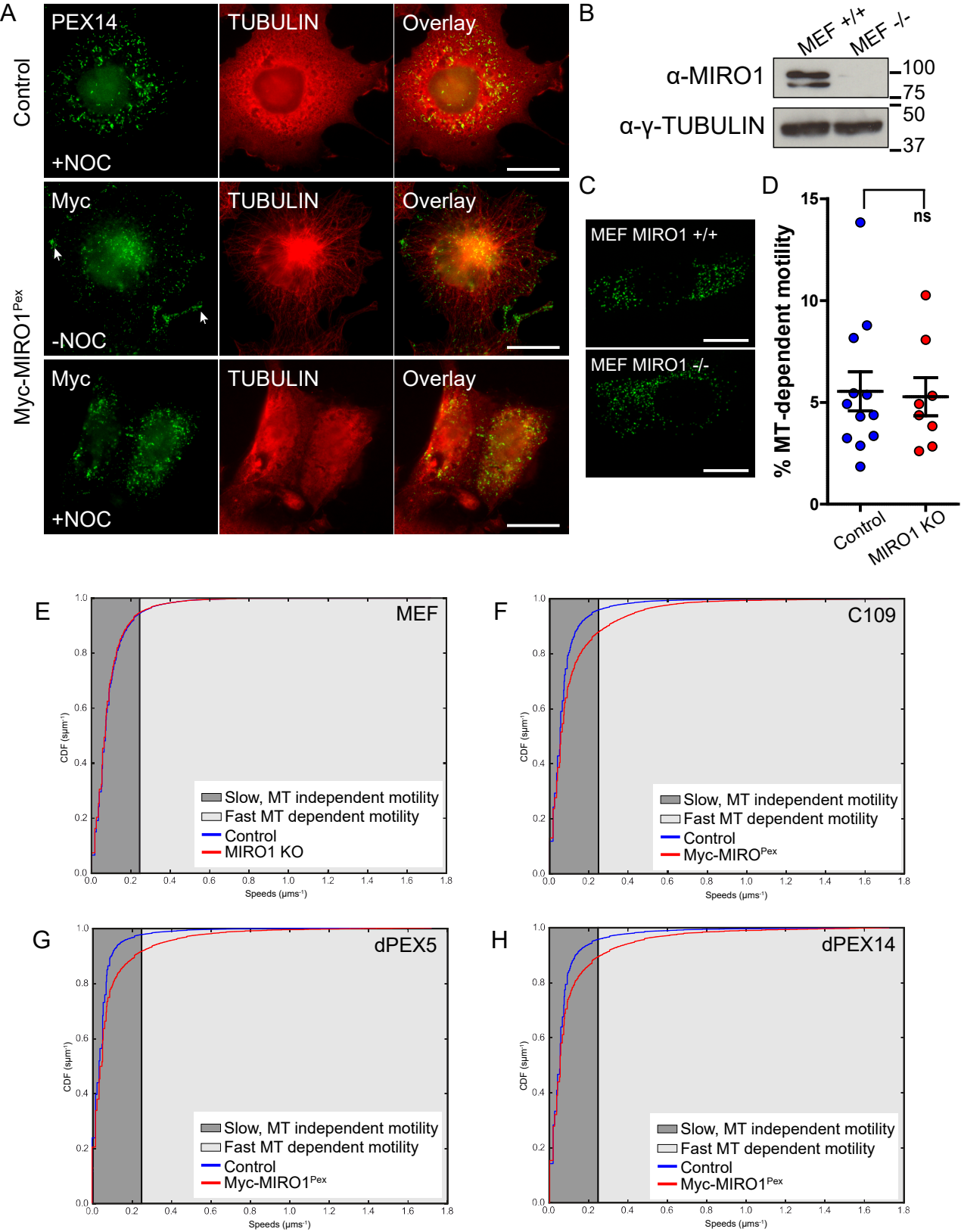
A
Control
Myc-MIRO1Pex
PEX14
TUBULIN
Overlay
+NOC
Myc
-NOC
B
MEF +/+
MEF -/-
α-MIRO1
α-γ-TUBULIN
100
75
50
37
C
MEF MIRO1 +/+
MEF MIRO1 -/-
D
% MT-dependent motility
ns
Control
MIRO1 KO
E
MEF
F
C109
G
dPEX5
H
dPEX14
CDF (sμm⁻¹)
Speeds (μms⁻¹)
Slow, MT independent motility
Fast MT dependent motility
Control
MIRO1 KO
Myc-MIRO1Pex